Monthly Notices of the ROYAL ASTRONOMICAL SOCIETY

MNRAS **540,** 2535–2554 (2025) https://doi.org/10.1093/mnras/staf819
Advance Access publication 2025 May 19

Tracing the formation and migration history: molecular signatures in the atmosphere of misaligned hot Jupiter WASP-94 A b using *JWST* NIRSpec/G395H

Eva-Maria Ahrer [1★] Siddharth Gandhi [2,3] Lili Alderson [4] James Kirk [5] Johanna Teske [6,7] Richard A. Booth [8] Catriona H. McDonald [9] Duncan A. Christie [1] Alastair B. Claringbold [2,3] Rebecca Nealon [2,3] Vatsal Panwar [2,3] Dimitri Veras [2,3,10] Hannah R. Wakeford [11] Peter J. Wheatley [2,3] and Maria Zamyatina [12]

[1]*Max-Planck-Institut für Astronomie, Königstuhl 17, D-69117 Heidelberg, Germany*
[2]*Centre for Exoplanets and Habitability, University of Warwick, Gibbet Hill Road, Coventry CV4 7AL, UK*
[3]*Department of Physics, University of Warwick, Gibbet Hill Road, Coventry CV4 7AL, UK*
[4]*Department of Astronomy, Cornell University, 122 Sciences Drive, Ithaca, NY 14853, USA*
[5]*Department of Physics, Imperial College London, Prince Consort Road, London SW7 2AZ, UK*
[6]*Earth and Planets Laboratory, Carnegie Institution for Science, 5241 Broad Branch Road NW, Washington, DC 20015, USA*
[7]*The Observatories of the Carnegie Institution for Science, 813 Santa Barbara St, Pasadena, CA 91101, USA*
[8]*School of Physics and Astronomy, University of Leeds, Leeds LS2 9JT, UK*
[9]*Institute of Astronomy, University of Cambridge, Madingley Road, Cambridge CB3 0HA, UK*
[10]*Centre for Space Domain Awareness, University of Warwick, Gibbet Hill Road, Coventry CV4 7AL, UK*
[11]*School of Physics, University of Bristol, HH Wills Physics Laboratory, Tyndall Avenue, Bristol BS8 1TL, UK*
[12]*Department of Physics and Astronomy, Faculty of Environment, Science and Economy, University of Exeter, Exeter EX4 4QL, UK*

Accepted 2025 May 16. Received 2025 May 12; in original form 2025 April 1

ABSTRACT

The discovery of hot Jupiters that orbit very close to their host stars has long challenged traditional models of planetary formation and migration. Characterizing their atmospheric composition – mainly in the form of the carbon-to-oxygen (C/O) ratio and metallicity – can provide insights into their formation locations and evolution pathways. With *JWST*, we can characterize the atmospheres of these types of planets more precisely than previously possible, primarily because it allows us to determine both their atmospheric oxygen and carbon composition. Here, we present a *JWST* NIRSpec (Near-Infrared Spectrograph)/G395H transmission spectrum from 2.8 to 5.1 μm of WASP-94 A b, an inflated hot Jupiter with a retrograde misaligned orbit around its F-type host star. We find a relatively cloud-free atmosphere, with absorption features of H_2O and CO_2 at detection significances of $\sim 4\sigma$ and $\sim 11\sigma$, respectively. In addition, we detect tentative evidence of CO absorption at $\sim 3\sigma$, as well as hints of sulphur with the detection of H_2S at a $\sim 2.5\sigma$ confidence level. Our favoured equilibrium chemistry model determines a C/O ratio of $0.49^{+0.08}_{-0.13}$ for WASP-94 A b's atmosphere, which is substellar compared to the star's C/O ratio of 0.68 ± 0.10. The retrieved atmospheric metallicity is similar to the star's metallicity, as both are $\sim 2\times$ solar. We find that this substellar C/O ratio and stellar metallicity can be best explained by pebble accretion or planetesimal accretion in combination with large-distance migration of the planet.

Key words: exoplanets – planets and satellites: atmospheres – planets and satellites: gaseous planets – planets and satellites: individual: WASP-94 A b.

1 INTRODUCTION

JWST has already started to revolutionize our understanding of exoplanet atmospheres, allowing us to study their composition in the infrared at high precision and explore new chemical processes, e.g. the detection of photochemically produced sulphur dioxide in the atmosphere of exoplanet WASP-39 b (Alderson et al. 2023; Rustamkulov et al. 2023; Tsai et al. 2023). In transmission spectroscopy, precise measurements of the exoplanet transit depth as a function of wavelength are used to reveal the opacity sources acting in the planetary atmosphere (e.g. Charbonneau et al. 2002). Extending transmission spectra further into the infrared provides access to many additional molecules, in particular enabling observations of carbon species in exoplanet atmospheres. Hot Jupiters are ideal targets for atmospheric observations as they tend to have large atmospheric scale heights, due to high temperatures and large radii, resulting in strong features in transmission spectra.

JWST transmission spectra have revealed a range of molecular species in the sample of hot Jupiters (here defined as exoplanets with temperatures 1000–2000 K, radii $R_p > 0.5\ R_{Jup}$, and masses $M_p > 0.2\ M_{Jup}$) published thus far, demonstrating the diversity of hot

★ E-mail: ahrer@mpia.de

Jupiter atmospheres. The detections range from carbon- and oxygen-bearing species, such as water vapour (e.g. Ahrer et al. 2023; Bell et al. 2023a; Feinstein et al. 2023; Radica et al. 2023; Taylor et al. 2023; Fu et al. 2024; Kirk et al. 2025; Louie et al. 2025), carbon dioxide (e.g. Alderson et al. 2023; JWST Transiting Exoplanet Community Early Release Science Team 2023; Rustamkulov et al. 2023; Xue et al. 2024), carbon monoxide (e.g. Esparza-Borges et al. 2023; Grant et al. 2023a), to sulphur species like sulphur dioxide (e.g. Alderson et al. 2023; Rustamkulov et al. 2023; Fu et al. 2024; Kirk et al. 2025) and hydrogen sulphide (Fu et al. 2024). Further discoveries in hot Jupiter atmospheres include the detection of individual cloud species, silicate clouds, using the mid-infrared detector MIRI (Mid-Infrared Instrument; e.g. Grant et al. 2023b; Inglis et al. 2024).

Hot Jupiters are prime targets for atmospheric studies, while they are also important for research into planet formation and migration, as both of these aspects are not fully understood. Leading planet formation theories such as core accretion (e.g. Pollack et al. 1996) and gravitational instability (e.g. Boss 1997) struggle to explain the formation of gas giants this close to their host stars where hot Jupiters are currently situated now (e.g. Rafikov 2005, 2006): core accretion theory struggles as it cannot form a large enough core for runaway gas accretion, and gravitationally unstable discs can only cool fast enough to fragment beyond several tens of astronomical unit (au; e.g. see review in Dawson & Johnson 2018). Instead, they likely formed further out in the protoplanetary disc (via either formation pathway) and migrated inwards, either via disc-driven migration or high-eccentricity migration (e.g. Goldreich & Tremaine 1980; Lin, Bodenheimer & Richardson 1996; Rasio et al. 1996; Weidenschilling et al. 1996).

To understand the dynamical history of hot Jupiters, we can investigate the distribution of alignments between the orbital planes of planets and the stellar spin axis of their host stars. For example, it has been suggested that low obliquities (near alignment of these two planes) point to disc-driven migration, while high obliquities point to high-eccentricity migration (e.g. Fabrycky & Winn 2009). However, there is evidence for tides damping obliquities after the initial stages of planet formation/migration, so low obliquity measurements do not necessarily mean disc-driven migration (e.g. Albrecht, Dawson & Winn 2022), in particular for older systems. Recent evidence also suggests that resonance locking could also drive damping of obliquities (as well as orbital eccentricity and semimajor axis; Zanazzi, Dewberry & Chiang 2024). Hence, it is generally not possible to trace a planet's migration history simply from its measured obliquity unless the host star is located above the Kraft break (Kraft 1967). The Kraft break denotes the separation in rotational velocity between hotter stars (quickly rotating) and cooler stars with a thick convective envelope (e.g. Dawson 2014; Albrecht et al. 2022). Tidal realignment is significantly more effective for cooler stars due to either the convective envelopes below the Kraft break (e.g. Albrecht et al. 2012) or stellar gravity modes (Zanazzi et al. 2024). Vice versa is also true: the host stars with radiative envelopes above the Kraft break are less likely to have realigned their hot Jupiter companions, and as such, they retain their primordial obliquities. Therefore, measured obliquities of hot Jupiters around hotter stars ($T_{\rm eff} \geq 6000$ K) may allow a distinction between the two migration mechanisms to be made: misaligned orbits are caused by high-eccentricity migration and aligned orbits point to disc-driven migration (e.g. Kirk et al. 2024a; Penzlin et al. 2024).

It has also been suggested that the atmospheric compositions of hot Jupiters can give clues about where and how they formed (e.g. Öberg, Murray-Clay & Bergin 2011; Madhusudhan, Amin & Kennedy 2014; Booth et al. 2017; Notsu et al. 2020; Schneider & Bitsch 2021; Penzlin et al. 2024). This approach is rooted in the fact that the composition of gas and solids in a protoplanetary disc varies radially as different volatiles occur in different states of matter due to temperature variations within the disc. Most recently, Penzlin et al. (2024) simulated the disc chemistry and migration of hot Jupiters, and one of their main conclusions is that hot Jupiters with solar to supersolar metallicity have accreted substantial amounts of rocky material. In addition, their carbon-to-oxygen (C/O) ratios are dependent on the method of migration: hot gas giants that migrated within the disc are expected to have a lower C/O (accretion of inner disc material) compared to those that underwent high-eccentricity migration after disc dispersal (see also Kirk et al. 2024a). Interestingly, the relative C/O trend between misaligned and aligned planets may be reversed if silicate evaporation is taking place. Probing these predictions by characterizing a sample of hot Jupiter atmospheres orbiting stars above the Kraft break is the primary goal of a larger, future study.

Here we contribute an additional planet to this study, WASP-94 A b, a hot Jupiter orbiting a star above the Kraft break in a misaligned, retrograde orbit. We present *JWST* Near-Infrared Spectrograph (NIRSpec)/G395H observations of this planet, targeted by the *JWST* programme GO 3154 (PI: Ahrer). First, we introduce the system in Section 2, followed by a description of the observations and the data analysis in Section 3. The atmospheric retrieval analysis is described in Section 4, and we discuss our results in Section 5. We conclude this paper with our findings in Section 6. Additional figures can be found in Appendices A, B, C, and D.

2 THE WASP-94 SYSTEM

The WASP-94 system consists of two F-type stars, WASP-94 A (F8) and WASP-94 B (F9), with V magnitudes of 10.1 and 10.5, respectively. Their angular separation is 15.03 ± 0.01 arcsec with an orbital separation estimated to be >2700 au (Neveu-Vanmalle et al. 2014). One confirmed planet around each star (Neveu-Vanmalle et al. 2014) was discovered as part of the Wide Angle Search for Planets (WASP) survey (Pollacco et al. 2006). Both planets orbiting the two stars in the WASP-94 system are hot Jupiters. WASP-94 A b is a transiting exoplanet studied in this work, while WASP-94 B b does not transit and has been detected by radial velocity measurements only. Therefore, we cannot determine whether WASP-94 B b is in a similar or different orbit to WASP-94 A b or follow-up with atmospheric studies. The stellar parameters for WASP-94 A are summarized in Table 1 and the system's architecture is sketched in Fig. 1.

WASP-94 A b's radius was reported as $1.72^{+0.06}_{-0.05}\,R_{\rm Jup}$ (Neveu-Vanmalle et al. 2014) and later refined as $1.58 \pm 0.13\,R_{\rm Jup}$ with the first *Gaia* parallaxes (Stassun, Collins & Gaudi 2017). As the star's radius has been further refined with *Gaia* Data Release 3 (DR3; see Table 2; Andrae et al. 2023; Gaia Collaboration 2023), we adopt the planetary radius calculated by the weighted mean of our transit depth measurements multiplied by the DR3 stellar radius in our atmospheric retrieval studies. The mass of WASP-94 A b was found as $0.452^{+0.035}_{-0.032}\,M_{\rm Jup}$ (Neveu-Vanmalle et al. 2014) and the orbit is consistent with zero eccentricity (Bonomo et al. 2017). An equilibrium temperature of 1508 ± 75 K was derived using *Spitzer* eclipses (Garhart et al. 2020), which were also consistent with the previously derived circular orbit. Most interestingly, WASP-94 A b is in a retrograde, misaligned orbit around its host star, tightly constrained with recent High Accuracy Radial velocity Planet Searcher (HARPS) measurements of its projected obliquity $\lambda = -123.0 \pm 3.0$ (Ahrer et al. 2024). We discuss the observed orbit of WASP-94 A b

Table 1. Stellar and planetary parameters for the WASP-94 A planetary system. References are as follows: [1] Høg et al. (2000); [2] Skrutskie et al. (2006, 2MASS); [3] Neveu-Vanmalle et al. (2014); [4] Teske, Khanal & Ramírez (2016) from a differential analysis with WASP-94 B; [5] Bonomo et al. (2017); [6] Gaia Collaboration (2023, *Gaia* DR3); and [7] Andrae et al. (2023, *Gaia* DR3 GSP-Phot).

Stellar parameters of WASP-94 A		
Parameter	Value	Reference
Brightness, $V_{\rm mag}$	10.05 ± 0.04	[1]
Brightness, $J_{\rm mag}$	9.159 ± 0.027	[2]
Brightness, $K_{\rm s,mag}$	8.874 ± 0.024	[2]
Spectral type	F8	[3]
Effective Temperature, $T_{\rm eff}$ (K)	6194 ± 5	[4]
Age (Gyr)	2.55 ± 0.25	[4]
Surface gravity, $\log g$ ($\log_{10}$ (cm s^{-2}))	4.210 ± 0.011	[4]
Metallicity [Fe/H] (dex)	0.320 ± 0.004	[4]
Mass, M_* ($M_\odot$)	1.450 ± 0.090	[2], [5]
Radius, R_* ($R_\odot$)	$1.5784^{+0.0095}_{-0.0110}$	[6], [7]

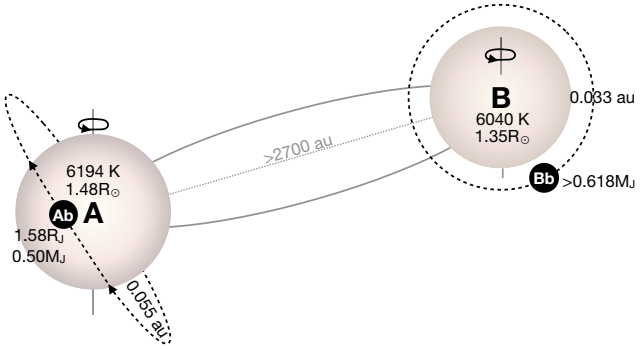

Figure 1. Sketch of the WASP-94 system. On the left, WASP-94 A b is shown orbiting its host star at 0.056 au in a misaligned, retrograde orbit. On the right, the non-transiting WASP-94 B b orbits its host star at 0.033 au. Both stars are F-type stars and are at least >2700 au apart. Only WASP-94 A and WASP-94 A b's radii ($R_{\rm p}/R_*$) are to scale.

and its implications for planet formation and migration within a stellar binary in Section 5.2.

In Teske et al. (2016), the authors took advantage of the 'twin' nature of WASP-94 A and WASP-94 B to conduct a stellar abundance analysis looking for compositional anomalies that might indicate differences in how planet formation proceeded around each star, which is suggested by the retrograde and misaligned orbit of WASP-94 A b. Based on their high precision, strictly differential abundance analysis, Teske et al. (2016) found a slight depletion of volatile elements (∼−0.02 dex on average) but enhancement of refractory elements (∼0.01 dex) in WASP-94 A versus WASP-94 B. Whether or not these anomalies between the twin stars are actually related to planet formation is unclear. We revisit the abundance measurements of WASP-94 A in Section 5.

WASP-94 A b's atmosphere has been previously studied at low spectral resolution with the ESO Faint Object Spectrograph and Camera 2 spectrograph on the New Technology Telescope as part of the Low Resolution Ground-Based Exoplanet Atmosphere Survey using Transmission Spectroscopy, as well as at high spectral resolution with the HARPS spectrograph (Mayor et al. 2003), both located at La Silla, Chile. Ahrer et al. (2022) presented a low-resolution transmission spectrum of WASP-94 A b from 4020–7140 Å, showing evidence for a scattering slope and detecting Na absorption. Ahrer et al. (2024) found comparable Na signatures using the high spectral resolution of HARPS by resolving the Na doublet in the in-transit observations of WASP-94 A b.

3 DATA REDUCTION AND ANALYSIS

We analyse our new *JWST* NIRSpec/G395H observations using three independent reductions (EUREKA!, TIBERIUS, and EXOTIC-JEDI) to ensure our results are robust against reduction choices. We outline these in this section after a description of our observational set-up.

3.1 Observations

Our *JWST* observations of WASP-94 A b (GO 3154, PI: Ahrer) took place on 2024 June 7 using NIRSpec's highest resolution grism G395H/F290LP. We used 21 groups per integration, NRSRAPID readout mode, with 1451 total integrations and an overall exposure time of 8 h. The visit covered a total time of 2.25 h of pre-transit time, a transit time of 4.5 h (including ingress and egress), and a post-transit time of 1.25 h. Target acquisition was done using a fainter star (2MASS J20550897−3408314) within the splitting distance, using SUB32 subarray, three groups/integration, *F*140*X* filter, and NRSRAPID readout.

3.2 EUREKA!

We reduced the WASP-94 A b's observations using the open-source PYTHON package EUREKA! (Bell et al. 2022) that has been successfully applied to a multitude of observations (e.g. Ahrer et al. 2023; Bell et al. 2023b; Fu et al. 2024).

Table 2. The retrieved system parameters for the transit of WASP-94 A b from the *JWST* NIRSpec/G395H white light curves as fitted by the individual reductions.

Pipeline	Detector	T_0 (BJD)	$R_{\rm p}/R_*$	a/R_*	i (°)
EUREKA!	NRS1	245 60469.308647 ± 0.000019	0.10608 ± 0.00011	7.235 ± 0.018	88.42 ± 0.11
EUREKA!	NRS2	245 60469.308671 ± 0.000033	0.10560 ± 0.00060	7.279 ± 0.031	88.70 ± 0.24
EUREKA!	Weighted mean	245 60469.308656 ± 0.000017	0.10606 ± 0.00011	7.246 ± 0.016	88.47 ± 0.10
TIBERIUS	NRS1	245 60469.308645 ± 0.000019	0.106022 ± 0.000039	7.252 ± 0.016	88.54 ± 0.09
TIBERIUS	NRS2	245 60469.308666 ± 0.000028	0.105583 ± 0.000058	7.284 ± 0.024	88.71 ± 0.16
TIBERIUS	Weighted mean	245 60469.308652 ± 0.000016	0.105885 ± 0.000032	7.262 ± 0.013	88.58 ± 0.08
EXOTIC-JEDI	NRS1	246 0469.308631 ± 0.000019	0.105798 ± 0.000039	7.255 ± 0.016	88.57 ± 0.10
EXOTIC-JEDI	NRS2	246 0469.308651 ± 0.000027	0.105502 ± 0.000055	7.276 ± 0.022	88.67 ± 0.15
EXOTIC-JEDI	Weighted mean	246 0469.308638 ± 0.000016	0.105699 ± 0.000032	7.262 ± 0.013	88.601 ± 0.084

3.2.1 *Light-curve extraction*

To extract the time series stellar spectra, we started with the uncalibrated `uncal.fits` files and ran EUREKA!'s Stages 1 and 2, which are wrapped around the default JWST pipeline. We followed the default JWST steps in both stages, with the exception of the jump step where we used a threshold of 10σ (instead of the default 4σ), and we skipped the `photom_step`. In addition, we applied EUREKA!'s group-level background subtraction to reduce the $1/f$ noise by subtracting a zero-order polynomial after masking the trace and outliers >5 times the median. A custom bias scale factor was also used by computing a smoothing filter (see also Moran et al. 2024).

We extracted the stellar time series spectra in EUREKA!'s Stage 3. First, we performed a trace curvature correction, followed by a column-by-column background subtraction. For the background subtraction, we used a zero-order polynomial fitted to each column, excluding the area within 10 pixels of the centre of the trace and masking outliers with thresholds of 5σ along the time and the spatial axis. Finally, we extracted the time series spectra using an aperture size of 9 pixels.

We used Stage 4 of EUREKA! to generate binned spectroscopic light curves of our observations, as well as broad white-light light curves of the full NRS1 (2.8–3.7 μm) and NRS2 (3.8–5.2 μm) wavelength ranges. Prior to Stage 4, we manually masked one bad wavelength column in NRS2 and one in NRS1, which we found were not masked during Stage 3 and introduced outliers in the light curves and subsequently in the transmission spectrum. In EUREKA!'s Stage 4, we utilized a 5σ clipping with a 20-pixel rolling median to mask outliers in the light curves.

For all our reductions, we use two different binning schemes when generating our light curves, at a resolution of $R = 100$ and 400. This allows us to test our atmospheric inferences at different resolutions and determine whether there are outlier spectral channels that are binned over in the lower resolution data, while also resolving features in the planet's atmosphere. This follows the recommended strategy by the in-depth study of WASP-39 b using *JWST*'s NIRSpec/G395H, NIRSpec/PRISM, NIRCam/*F*322W2, and Near-Infrared Imager and Slitless Spectrograph/Single Object Slitless Spectroscopy (NIRISS/SOSS; Carter et al. 2024) and is commonly used in other *JWST* observations of hot Jupiters (e.g. Kirk et al. 2025; Meech et al. 2025).

3.2.2 *Light-curve fitting*

EUREKA!'s Stage 5 performs the light-curve fitting. First, we fit the white light curve for both NRS1 and NRS2 separately, freely fitting for the orbital parameters time of mid-transit (T_0), scaled semimajor axis (a/R_*), inclination (i), transit depth (R_p/R_*), as well as two parameters to fit a linear trend and one limb darkening parameter ($u2$). We used the quadratic limb darkening law and fixed the second parameter, $u1$, to the value calculated using the EXOTIC-LD tool (Grant & Wakeford 2024) and a 3D stellar atmosphere grid (Magic et al. 2015) based on the stellar parameters in Table 1. We fix the orbital period of WASP-94 A b to 3.9502001 d (Kokori et al. 2023).

For all light-curve fitting, we utilize the BATMAN package for our transit model and the Markov chain Monte Carlo package EMCEE (Foreman-Mackey et al. 2013) to retrieve our fitted parameters. The fitted values from the white light curve for NRS1 and NRS2 are summarized in Table 2, the fit is shown in Fig. 2.

For the spectroscopic light-curve fits, we fixed the parameters i, a/R_*, and T_0 to the retrieved values from the white light-curve fits. Therefore, only R_p/R_*, $u2$, and the two linear trend parameters are freely fitted for each spectroscopic light curve. The spectroscopic light curves at a spectral resolution of $R = 400$ are shown in Fig. 3.

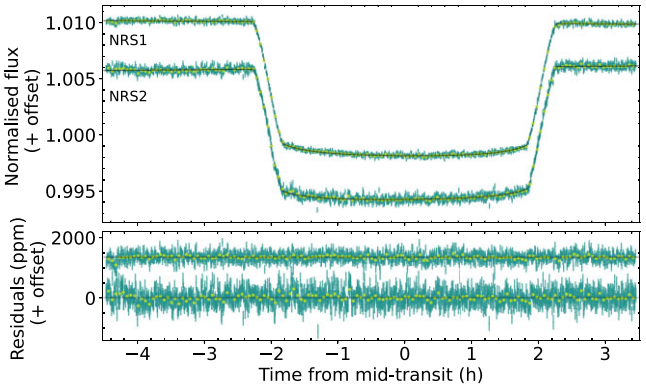

Figure 2. Top: Broad-band light curves of the transit of WASP-94 A b for the two NIRSpec detectors, NRS1 and NRS2, using the EUREKA! reduction. The black line denotes the fit to the data, while the light and darker data represent the unbinned and binned data (10-pixel binning), respectively. Bottom: Respective residuals of the fit to the light curves from the top panel.

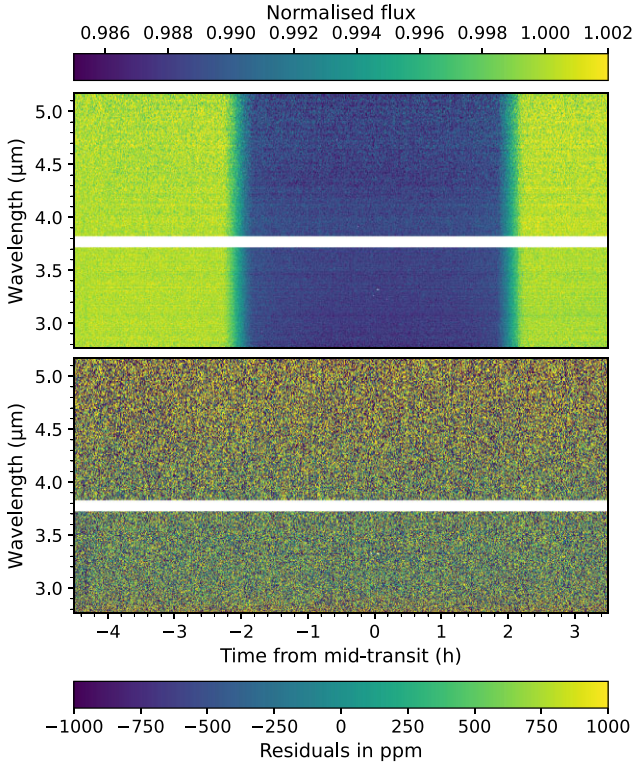

Figure 3. Light curves of WASP-94 A b's transit and corresponding residuals using EUREKA! at $R = 400$ for both NRS1 and NRS2 detectors.

3.3 TIBERIUS

For our second independent reduction of the data, we used TIBERIUS (Kirk et al. 2017, 2021) that has been used in several *JWST* analyses to date (e.g. JWST Transiting Exoplanet Community Early Release Science Team 2023; Rustamkulov et al. 2023; Kirk et al. 2024b; Meech et al. 2025).

3.3.1 Light-curve extraction

Our light-curve extraction proceeded in an identical way to that presented in Kirk et al. (2025). In brief, we process the `uncal.fits` files through Stage 1 of the JWST pipeline and then feed the resulting `gainscalestep.fits` files into TIBERIUS. The only difference between Kirk et al. (2025) and our application of TIBERIUS here is that we made a fresh bad pixel mask. This was motivated by potential changes in pixel behaviour between the different observation epochs. While we use the same reference files as Kirk et al. (2025), our custom step to flag outliers has the ability to identify pixels that would be outliers in one observation and not another.

3.3.2 Light-curve fitting

For our light-curve fitting, we adopted the same procedure as for the analysis of WASP-15 b (Kirk et al. 2025). Specifically, our light-curve model consisted of an analytic BATMAN (Kreidberg 2015) transit light curve multiplied by a linear-in-time polynomial. The parameter space was explored with a Levenberg–Marquadt algorithm within the SCIPY library (Virtanen et al. 2020). Our fits were performed in two iterations, with the first iteration used to rescale the photometric uncertainties by a factor of 1.4 to give $\chi^2_\nu = 1$. The second iteration was used to infer the best-fitting parameters and uncertainties.

We began by fitting the white light curves to derive a common set of system parameters. Similarly to the EUREKA! reduction, the free parameters here were the time of mid-transit (T_0), the scaled semimajor axis (a/R_*), the planet's orbital inclination (i), the scaled planet radius (R_p/R_*), and the two coefficients of the linear polynomial. We fixed the period to 3.9502001 d (Kokori et al. 2023). Similar to the EUREKA! reduction, we parametrized the limb darkening with a quadratic law, though with both limb darkening coefficients fixed to values computed using EXOTIC-LD (Grant & Wakeford 2024), 3D stellar atmosphere models (Magic et al. 2015), and the stellar parameters of Bonomo et al. (2017).

The best-fitting system parameters are given in Table 2, and we find these are consistent between the detectors. We then fitted the spectroscopic light curves with a/R_*, i, and T_0 fixed to the mean-weighted values from our white light fits. This meant that only R_p/R_* and the two coefficients of the linear polynomial were fit parameters.

We find minimal red noise in both the fits to the white and spectroscopic light curves, which allows us to obtain a precise transmission spectrum, with a median uncertainty of 37 and 71 ppm at $R = 100$ and 400, respectively.

3.4 EXOTIC-JEDI

Our third independent reduction uses EXOTIC-JEDI (Alderson, Grant & Wakeford 2022). Our reduction followed the same process as previous EXOTIC-JEDI reductions of other data sets (e.g. Alderson et al. 2023, 2024, 2025; May et al. 2023), treating NRS1 and NRS2 separately.

3.4.1 Light-curve extraction

We begin with the `uncal` files in Stage 1, a modified version of the JWST pipeline (v1.14.0; Bushouse et al. 2024), performing linearity, dark current, saturation, and ramp jump corrections (with a threshold of 15σ, as opposed to the default 4σ), the EXOTIC-JEDI custom destriping routine to remove $1/f$ noise at the group level, the EXOTIC-JEDI custom bias subtraction, and finally ramp fitting. In Stage 2, we performed the standard temporal and spatial pixel outlier cleaning and further $1/f$ and background removal. To extract the 1D stellar spectra, we used an aperture region five times the full width at half-maximum of Gaussians fitted to each column of the spectral trace, equivalent to approximately 7 pixels from edge to edge. We additionally cross-correlated the resulting spectra to obtain x- and y-pixel positional shifts to be used as systematic detrending parameters in our light-curve fits.

3.4.2 Light-curve fitting

We fitted white light curves for NRS1 and NRS2 across the G395H wavelength range (2.814–3.717 and 3.824–5.111 μm, respectively), which were used to inform the spectroscopic light curve fits. For the white light curves, we fitted for R_p/R_*, i, a/R_*, and T_0, holding the period fixed to the value presented in Neveu-Vanmalle et al. (2014). We calculated and held fixed stellar limb darkening coefficients using EXOTIC-LD (Grant & Wakeford 2024), with the non-linear limb darkening law (Claret 2000) using the Magic et al. (2015) 3D stellar models and stellar parameters from Stassun et al. (2017). We used a least-squares optimizer to fit for a Kreidberg (2015) transit model simultaneously with a systematic model $S(\lambda)$ of the form

$$S(\lambda) = s_0 + (s_1 \times t) + (s_2 \times x_s|y_s|),$$

where x_s is the x-positional shift of the spectral trace, $|y_s|$ is the absolute magnitude of the y-positional shift of the spectral trace, t is the time, and s_0, s_1, s_2 are coefficient terms. During the fitting process, we removed any data points that were greater than 4σ outliers in the residuals and refitted the light curves until no such points remained. We additionally rescaled the light-curve errors using the beta value (Pont, Zucker & Queloz 2006) to account for any remaining red noise in the data.

The spectroscopic light curves were fitted in the same manner as the white light curves, however, we held a/R_*, i, and T_0 fixed to the corresponding white light-curve value for each detector as appropriate (see Table 2). We used the same $R = 100$ and 400 binning schemes as the EUREKA! and TIBERIUS reductions, as shown in Fig. 4. Note that the EXOTIC-JEDI reduction does not include the bluest wavelength bins in NRS1 (see Fig. 4) as the throughput curve used in the computation of the limb darkening values with EXOTIC-LD does not cover wavelengths <2.814 μm, while EUREKA! and TIBERIUS reductions use an extrapolated throughput towards the bluer wavelength ranges. The official throughput files for G395H, as provided by STScI G395H do not cover those bluer wavelengths, and any information outside of the computed throughput of the instrument cannot be accurately assigned to any single wavelength and is potentially a combination of spectral wavelengths exposed on those pixels of the detector. So, not using wavelength <2.814 μm is a more conservative approach.

3.5 Transmission spectra and limb asymmetries

The resulting transmission spectra using NIRSpec/G395H for WASP-94 A b from all three reductions, EUREKA!, TIBERIUS, and EXOTIC-JEDI, are shown in Fig. 4, at two spectral resolutions with $R = 100$ and 400 on the left and right panel, respectively, as well as their differences in the bottom panel. The data show visible absorption features of H_2O with the slope in the bluer end of the spectrum and CO_2 at ∼4.4 μm.

We additionally explore the possibility of limb asymmetries in our light curves using the EUREKA! $R = 100$ light curves with the open-source PYTHON package CATWOMAN (Jones & Espinoza 2020; Espinoza & Jones 2021) and the nested sampling algorithm DYNESTY (Speagle 2020). Asymmetries at the terminator region can arise from temperature differences and variations of chemical compositions on the morning and evening terminators of exoplanets, the presence of

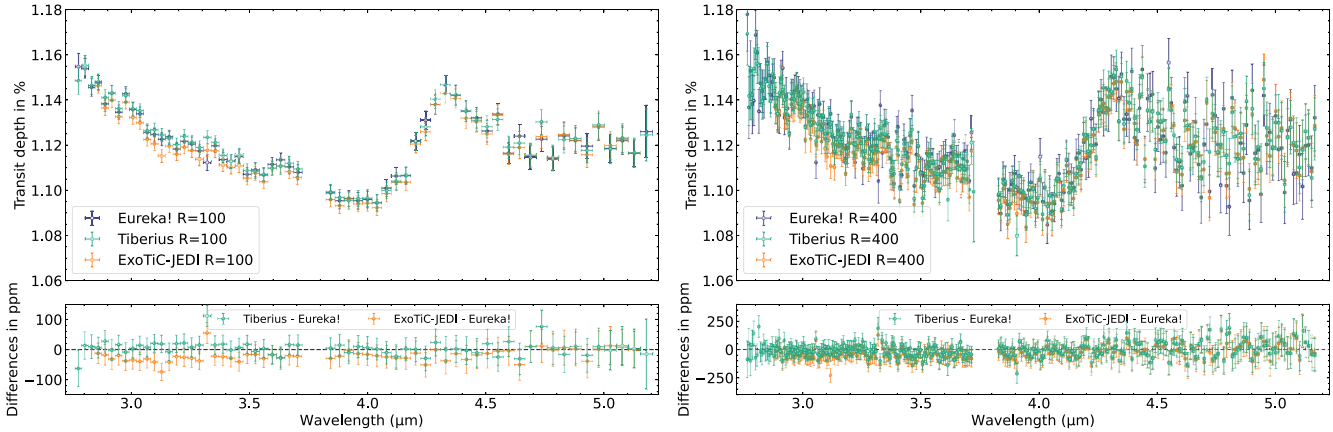

Figure 4. Top panels: Transmission spectrum of WASP-94 A b using *JWST*'s NIRSpec/G395H, using three independent reduction pipelines, TIBERIUS, EUREKA!, and EXOTIC-JEDI. The two panels show the spectra at two different binning schemes with $R = 100$ on the left and $R = 400$ on the right. Bottom panels: Differences between the reductions compared to EUREKA!. Note that the y-axis on the left panel is a different scale $(-150, +150)$ ppm compared to the right panel $(-400, +400)$ ppm for visual clarity. EXOTIC-JEDI displays a slight offset compared to TIBERIUS and EUREKA! in the NRS1 spectrum.

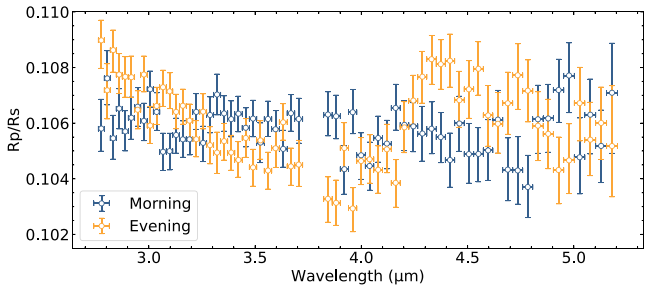

Figure 5. Morning and evening transmission spectrum of WASP-94 A b applying CATWOMAN (Jones & Espinoza 2020; Espinoza & Jones 2021) to the EUREKA! $R = 100$ light curves.

which has recently been demonstrated for hot gas giants using *JWST* (Espinoza et al. 2024; Murphy et al. 2024).

With CATWOMAN we modelled the transiting planet as two semi-circles with different radii. We fixed the orbital parameters for NRS1 and NRS2 as described in Table 2 and fixed the quadratic limb darkening coefficients to the values from EXOTIC-LD (Wakeford & Grant 2022; Grant & Wakeford 2024) as described before. We fit the transit mid-time for each bin (Gaussian prior, from Table 2) as well as the transit depths components as R_p/R_s for morning and evening side (uniform prior, 0.10–0.11) and an error inflation term. Before fitting with CATWOMAN, we remove the polynomial trend term found with the traditional light-curve fitting. Therefore, each spectroscopic bin is fitted using four free parameters: the morning and evening radius of the planet, mid-transit time, and the noise term. We run the nested sampling algorithm with a total of 400 live points (100× number of dimensions). We further fit the same model without asymmetries, i.e. assuming the morning and evening radius to be equal (so three free parameters), to allow for Bayesian evidence comparison.

The resulting morning and evening transmission spectra applying CATWOMAN to the EUREKA! $R = 100$ light curves are shown in Fig. 5. We find different spectra between the two limbs, however, when comparing the Bayesian evidence difference between the asymmetric morning–evening model and the conventional symmetric terminator model, the latter, less complex model is sufficient to fit the data (e.g. Jeffreys 1983; Trotta 2008). In fact, the Bayesian evidence favours the symmetric transit model in all spectroscopic bins, with differences $\Delta \ln \mathcal{Z}$ ranging from 0.5 to 1.5. The shape of the morning and evening spectra is consistent across reductions (see Appendix A). In a similar manner, the small differences in Bayesian evidence $\ln \mathcal{Z}$ hold true for TIBERIUS and EXOTIC-JEDI as well, favouring the simpler model. Future work may compare and contrast these potential limb asymmetries, but this is beyond the scope of this work.

4 ATMOSPHERIC RETRIEVAL ANALYSIS

We perform atmospheric retrievals using two independent retrieval codes – PRT and HYDRA – on our *JWST* transmission spectra of WASP-94 A b. We use PRT to run equilibrium chemistry retrievals as well as free chemistry retrievals with an isothermal temperature profile. We then employ the HYDRA retrieval set-up to investigate a non-isothermal profile and a more complex haze and cloud parametrization. We further test for an offset between the two detectors, NRS1 and NRS2.

4.1 PRT: free chemistry and equilibrium chemistry

We performed free chemistry and equilibrium chemistry retrievals with PETITRADTRANS (PRT) version 3 (Mollière et al. 2019; Nasedkin, Mollière & Blain 2024) on WASP-94 A b's transmission spectra, both for $R = 100$ and 400 of the *JWST* spectra for all three reductions. PRT explores the parameter space using the PYTHON version of the nested-sampling algorithm MULTINEST (Feroz, Hobson & Bridges 2009).

We included the following species using correlated k radiative transfer with opacity tables at $R = 1000$: H_2O, CO, CO_2, CH_4, H_2S, HCN, NH_3, and C_2H_2. The individual references for each species can be found in Appendix B, Table B1. We assume an H_2- and He-dominated atmosphere and include opacity from H_2–H_2 and H_2–He collision-induced absorption (Richard et al. 2012). The atmospheric pressures we consider range from 10^{-8} to 10^{2} bar.

For the cloud parametrization, we include a grey cloud deck with the cloud-top pressure as a free parameter. We fit for reference pressure and planet mass using a Gaussian prior centred on the planet's mass ($0.456\ M_{Jup}$) with a standard deviation of $0.05\ M_{Jup}$, while we fix the planet radius to 0.106× the stellar radius (based on the white light-curve fit). We use a wide, uniform prior for the limb temperature. The stellar radius was fixed to $1.5784\ R_\odot$ (see Table 1). In the case of our free chemistry retrievals, we used priors for the individual log mass fractions of each species from −10 to 0. In the

Table 3. Bayesian evidences differences $\Delta \ln \mathcal{Z}$ for equilibrium and free chemistry retrieval set-ups with and without an offset between the two NIRSpec NRS1 and NRS2 detectors. The PRT values (both equilibrium and free chemistry) are relative to the favoured retrieval, which is the equilibrium chemistry set-up including the offset (indicated by '–', first column). Therefore, this also demonstrates that the equilibrium chemistry set-up with offset is preferred over the free chemistry. The two rightmost columns correspond to the $\Delta \ln \mathcal{Z}$ values for the HYDRA free chemistry set-up, relative to the set-up with an offset ('–'), also showing a preference for including an offset.

Reduction	PRT: equilibrium chemistry w/ offset	PRT: equilibrium chemistry w/o offset	PRT: free chemistry w/ offset	PRT: free chemistry w/o offset	HYDRA: free chemistry w/ offset	HYDRA: free chemistry w/o offset
EUREKA! $R = 100$	–	-5.2 ± 0.2	-2.7 ± 0.2	-7.3 ± 0.2	–	-3.2 ± 0.2
EUREKA! $R = 400$	–	-7.2 ± 0.2	-3.7 ± 0.2	-7.9 ± 0.2	–	-3.7 ± 0.2
TIBERIUS $R = 100$	–	-2.3 ± 0.2	-1.6 ± 0.2	-5.1 ± 0.2	–	-3.4 ± 0.2
TIBERIUS $R = 400$	–	-2.9 ± 0.2	-2.8 ± 0.2	-5.8 ± 0.2	–	-2.9 ± 0.2
EXOTIC-JEDI $R = 100$	–	-1.5 ± 0.2	-3.0 ± 0.2	-5.2 ± 0.2	–	-2.6 ± 0.2
EXOTIC-JEDI $R = 400$	–	-0.4 ± 0.2	-4.4 ± 0.2	-4.7 ± 0.2	–	-0.6 ± 0.2

equilibrium chemistry case, we used a uniform prior for the C/O ratio of 0.1–1.5 (varying the oxygen content) and a log-uniform prior of −2 to 3 for the metallicity (Fe/H × solar). For the runs where an offset between NRS1 and NRS2 was fit, we employed a uniform prior from −200 to +200 ppm. The priors of all parameters are summarized in Appendix B, Table B1. In total, including the offset, we fit 13 free parameters in the free chemistry and seven parameters in the equilibrium chemistry case.

4.2 HYDRA: free chemistry

We perform free-chemistry atmospheric retrievals with HYDRA (Gandhi et al. 2019, 2022). This assumes the volume mixing ratio (VMR) of each species is a free parameter. Our molecular opacities are calculated from pre-computed grids over a range of pressures and temperatures spanning the photosphere of WASP-94 A b. We include the same species as that for the PRT retrievals (H_2O, CO, CO_2, CH_4, H_2S, HCN, NH_3, and C_2H_2). The individual line lists we used are summarized along the priors in Appendix B, Table B1. In addition to sources of line opacity, we also include absorption from H_2–H_2 and H_2–He interactions (Richard et al. 2012).

The HYDRA retrieval includes six free parameters that determine the vertical thermal profile of the atmosphere, following the procedure by Madhusudhan & Seager (2009). We divide the atmosphere into 50 equal layers in log-space with pressures from 10^{-7} to 10^{2} bar. This allows for a range of non-inverted, inverted, and isothermal profiles driven by the observational constraints. We also include an additional parameter for the reference pressure at which the radius of WASP-94 A b is set. For cloud and haze contributions to the opacity, we include four additional parameters, including the cloud fraction, as discussed in Welbanks & Madhusudhan (2021) and Gandhi et al. (2022). Finally, we retrieve an offset between the two NIRSpec detectors, resulting in a total of 20 free parameters in the retrieval. Table B1 shows the prior ranges for each of the parameters. Our retrievals are performed using the MULTINEST nested-sampling algorithm (Feroz & Hobson 2008, 2013; Buchner et al. 2014), with the spectral model generated at $R = 100\,000$ and then convolved and binned to the data resolution.

5 RESULTS AND DISCUSSION

5.1 Atmospheric characterization of WASP-94 A b

For WASP-94 A b's atmosphere, we retrieve consistent parameters for mass and reference pressure across both chemical equilibrium and free chemistry retrievals and between the two retrieval codes.

Temperatures and cloud-top pressures varied between the chemical set-ups in PRT and HYDRA. In both the free chemistry retrievals, the temperatures are lower (≈200 K lower) and the cloud deck is at a higher pressure ($\Delta \log P_{\rm cloud} \sim 2$ bar, i.e. higher up in the atmosphere) compared to the equilibrium set-up. These two parameters are degenerate as to first-order the scale height (and thus the features) increases with temperature while the cloud-top pressure mutes the features when it decreases.

In all the equilibrium chemistry retrievals, we find a limb temperature of 900–1000 K across all reductions (with uncertainties of ≈100–200 K), which is lower than the equilibrium temperature. This is a common occurrence in 1D isothermal retrievals due to the unresolved limb asymmetries (MacDonald, Goyal & Lewis 2020) and/or from the pressure–temperature (*P*–*T*) profile parametrization (Welbanks & Madhusudhan 2022).

5.1.1 Evidence for an offset between NRS1 and NRS2

While NRS1 and NRS2 are the same type of detectors, they do exhibit performance differences. In addition, NRS1 is more often illuminated compared to NRS2, as NRS2 is not used for every observing mode, while NRS1 is. This results in differences in the systematics properties, e.g. as seen in time series observations where the NRS1 light curves show a stronger linear trend compared to the NRS2 equivalent. This is also the case for our data set, though with the deep transit of WASP-94 A b it is hardly visible in Fig. 2. Due to this effect, it has become common practice to test for detector offsets in the transmission spectrum by investigating the inclusion of an offset parameter in the atmospheric retrievals (e.g. May et al. 2023; Ohno et al. 2025; Alderson et al. 2025; Bello-Arufe et al. 2025; Schmidt et al. 2025).

With both PRT and HYDRA, we run retrievals for equilibrium and free chemistry, including and excluding an offset between NRS1 and NRS2 for all reductions at all resolutions. We find that in all cases the Bayesian evidence comparison favours the model with the offset over one without an offset, see Table 3. The values of the offset fitted by all retrievals agree well for all reductions and are of the order of 38–93 ppm; see Table 4.

The statistical significances of preference for an offset vary slightly across reductions and retrieval set-ups. The Bayesian evidence difference $\Delta \ln \mathcal{Z}$ ranges from 2.3 to 7.2 (2.95σ to 4.21σ) for the EUREKA! and TIBERIUS reductions, clearly favouring the retrievals with the offsets. The fitted offsets using the EUREKA! and TIBERIUS reductions also agree within their 1σ uncertainties. On the other hand, the retrievals on the EXOTIC-JEDI reductions do not show a clear preference, with model evidence differences of 0.3–1.5 ($<1\sigma$),

Table 4. Retrieved offsets between the two NIRSpec/G395H detectors, NRS1 and NRS2. In PRT, it is applied as a subtraction to the transit depths in NRS2, so the negative value indicates that NRS2 is shifted up in regards to NRS1. The full retrieval results for these runs are shown in Table C1.

	Retrieved offset between NRS1 and NRS2 in ppm		
Reduction	PRT eq. chem.	PRT free chem.	HYDRA
EUREKA! $R = 100$	-69 ± 15	-76 ± 18	-60 ± 17
EUREKA! $R = 400$	-87 ± 17	-93 ± 21	-74 ± 20
TIBERIUS $R = 100$	-60 ± 17	-80 ± 19	-64 ± 17
TIBERIUS $R = 400$	-57 ± 16	-76 ± 20	-57 ± 18
EXOTIC-JEDI $R = 100$	-52 ± 16	-69 ± 20	-57 ± 17
EXOTIC-JEDI $R = 400$	-47 ± 16	-52 ± 22	-37 ± 18

though still in favour of including offsets. In addition, all fitted offsets are inconsistent with a zero offset at a 2.1σ–3.5σ level.

We note that the C/O ratio and abundances in the chemical equilibrium and free chemistry, respectively, are affected by the choice of whether an offset is included or not. For example, the C/O ratio for our fiducial spectrum (EUREKA! $R = 400$) without an offset is $\mathrm{C/O} = 0.194 \pm 0.079$, whereas if we include an offset in the retrieval, the $\mathrm{C/O} = 0.49^{+0.08}_{-0.13}$. We also find evidence for CH_4 at a 4σ level, which seems unlikely for a planet at this temperature. Therefore, we urge the community to test detector offsets when running atmospheric retrievals on *JWST* NIRSpec/G395H observations.

In summary, we see a slight offset between the data reductions by eye in Fig. 4, the Bayesian evidence prefers the inclusion of an offset for all reductions at both resolutions and for all retrieval set-ups, and the fitted offsets are inconsistent with a zero at a 2.1σ–3.5σ level. We conclude that the inclusion of an offset between NRS1 and NRS2 is necessary, and therefore, all our fiducial models include an offset between NRS1 and NRS2.

5.1.2 C/O and metallicity

With our equilibrium chemistry retrieval analysis using PRT, we find the ratio between carbon and oxygen molecules in the atmosphere of WASP-94 A b to be subsolar to solar (ranging from 0.40 to 0.53, see Table 5) and consistent across reductions within their 1σ uncertainties; see Fig. 6. For the atmospheric metallicity of WASP-94 A b, we find slightly supersolar metallicities for all reductions and resolutions, ranging between 1.5 and 2.4 × solar.

For comparison, we computed the C/O ratio and metallicities for our best-fitting free chemistry models for all reductions and resolutions using HYDRA and PRT, summarized in Table 5 and

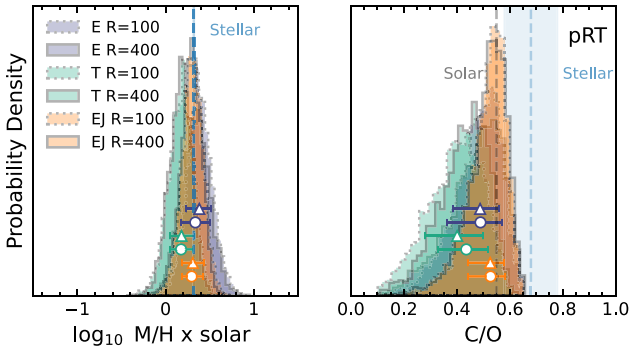

Figure 6. Retrieved metallicity and C/O constraints for WASP-94 A b from the equilibrium chemistry retrievals using PRT for each of the reductions at both binned spectral resolutions. The round circles and triangle shapes as markers correspond to the median value that was found for the $R = 100$ and 400 resolutions, respectively.

shown in Fig. 7. The two best-fitting free chemistry and equilibrium chemistry models using PRT are shown in Fig. 8. The numbers computed by HYDRA and PRT are consistent within $<1\sigma$ for both the C/O ratios and metallicity (as (C + O)/H × solar).

Across the board, we find that the C/O values in the HYDRA and PRT free chemistry retrievals are lower than the ones retrieved by the PRT chemical equilibrium retrievals, ranging from 0.10 to 0.32 versus 0.40 to 0.53, although the uncertainties on those computed values are relatively high and therefore consistent with the equilibrium chemistry model. In addition, using free chemistry abundances to compute C/O ratios may be biased towards lower C/O as features by carbon species such as CH_4 as well as HCH (and CO) are blended with the strong H_2O bands and are not fully spectrally resolved. Therefore, their abundances may be underestimated in free chemistry retrievals and contributing to a lower C/O ratio.

In contrast, the inferred metallicities are higher compared to the retrieved values by the equilibrium chemistry run. When comparing the VMRs (see Fig. 9), it is clear that the free chemistry retrievals show consistently higher abundances for all molecules compared to the equilibrium chemistry model. Therefore, the (C + O)/H will be higher for the free chemistry. The difference in abundances can be explained by the difference in cloud deck (see Table C1), where the equilibrium chemistry retrieval prefers the grey cloud deck to be higher up in the atmosphere and therefore muting the features.

Using the Bayesian evidence values for all atmospheric retrieval runs, we find that the equilibrium chemistry models are preferred

Table 5. Retrieved C/O ratios and metallicities of WASP-94 A b's atmosphere in the chemical equilibrium case (left) and the inferred values from the free chemistry retrievals (right), demonstrating that the equilibrium chemistry prefers higher C/O and lower metallicity. Solar refers to Asplund et al. (2009). The (C + O)/H (×solar) for all PRT equilibrium runs were computed using the in-built conversion to O/H and C/H, where the value stated here is using the median C/O and median metallicity for each reduction and the uncertainties stated here use both 1σ C/O and metallicity uncertainties to determine a conservative boundary (i.e. the upper error is derived using the highest (C + O)/H, with the $+1\sigma$ of metallicity (varying C) and the -1σ of C/O (varying O) and vice versa for the lower error). Note that Bayesian evidence favours the equilibrium chemistry models for all reductions.

	Equilibrium chemistry: PRT			Free chemistry: PRT		Free chemistry: HYDRA	
Reduction	C/O	Z (×solar)	(C + O)/H (×solar)	C/O	(C + O)/H (×solar)	C/O	(C + O)/H (×solar)
EUREKA! $R = 100$	$0.49^{+0.07}_{-0.10}$	$2.41^{+0.96}_{-0.65}$	$4.2^{+2.6}_{-1.4}$	$0.13^{+0.16}_{-0.09}$	24^{+36}_{-21}	$0.14^{+0.14}_{-0.07}$	6^{+13}_{-5}
EUREKA! $R = 400$	$0.49^{+0.08}_{-0.13}$	$2.17^{+0.96}_{-0.68}$	$3.8^{+2.8}_{-1.4}$	$0.19^{+0.24}_{-0.13}$	46^{+48}_{-36}	$0.09^{+0.22}_{-0.09}$	41^{+50}_{-25}
TIBERIUS $R = 100$	$0.40^{+0.10}_{-0.12}$	$1.52^{+0.54}_{-0.44}$	$3.0^{+2.2}_{-1.2}$	$0.10^{+0.13}_{-0.06}$	20^{+31}_{-16}	$0.13^{+0.12}_{-0.07}$	11^{+14}_{-8}
TIBERIUS $R = 400$	$0.44^{+0.08}_{-0.11}$	$1.50^{+0.48}_{-0.41}$	$2.79^{+1.7}_{-0.95}$	$0.14^{+0.15}_{-0.08}$	22^{+31}_{-18}	$0.17^{+0.16}_{-0.10}$	16^{+18}_{-11}
EXOTIC-JEDI $R = 100$	$0.526^{+0.054}_{-0.083}$	$2.04^{+0.65}_{-0.50}$	$3.38^{+1.6}_{-0.96}$	$0.25^{+0.24}_{-0.14}$	25^{+56}_{-24}	$0.21^{+0.17}_{-0.10}$	5^{+15}_{-5}
EXOTIC-JEDI $R = 400$	$0.527^{+0.056}_{-0.084}$	$1.97^{+0.59}_{-0.49}$	$3.28^{+1.4}_{-0.96}$	$0.32^{+0.23}_{-0.17}$	28^{+38}_{-25}	$0.33^{+0.22}_{-0.17}$	20^{+30}_{-16}

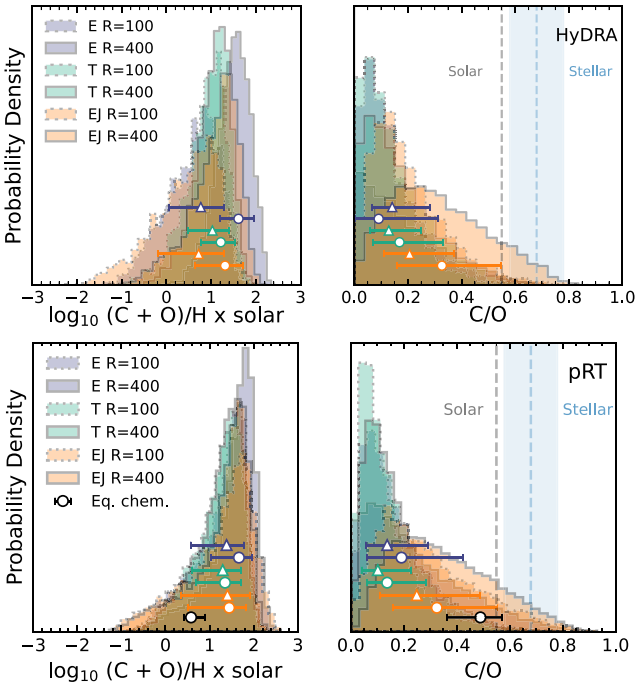

Figure 7. Derived metallicity as (C+O)/H compared to the solar (C + O)/H, and C/O constraints for WASP-94 A b from the two free chemistry retrievals: HYDRA (top) and PRT (bottom) for each of the reductions at both binned spectral resolutions. On the bottom panels, we also include the respective equilibrium chemistry values derived by PRT for EUREKA! $R = 400$.

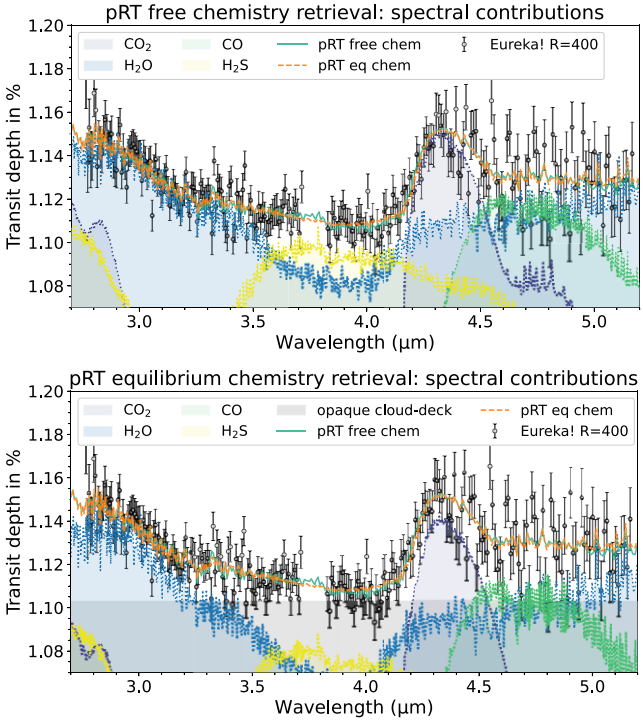

Figure 8. EUREKA! transmission spectrum of WASP-94 A b with the best-fitting PRT models using free chemistry and equilibrium chemistry and the fitted corresponding spectral contributions on the top and bottom panels, respectively. The best-fitting offset from the latter retrieval is applied to the NRS2 spectrum (87 ppm, consistent within 0.3σ with the 92 ppm from the free chemistry run). By eye the two models (equilibrium chemistry versus free chemistry) show remarkable agreement with the exception of the cloud deck which is at much higher altitudes for the equilibrium chemistry (see bottom panel), while the free chemistry retrieval prefers a cloud deck at lower altitudes not shown in the top panel as it is off the y-axis (equivalent of ∼1.05 per cent transit depth). However, the equilibrium chemistry retrieval runs were preferred across the board when comparing their Bayesian evidence values for all reductions and resolutions; see Table 3. Therefore, our favoured model is the equilibrium model, with $\Delta \ln \mathcal{Z} = 3.7$ (3.2σ) in the case of EUREKA! $R = 400$ using PRT.

across all reductions and all resolutions. This is visible in Table 3, where the PRT equilibrium chemistry runs are preferred over the more complex free chemistry runs with $\Delta \ln \mathcal{Z} = 1.6$–$4.4$. Thus, we do not detect evidence that points to disequilibrium processes in WASP-94 A b's atmosphere. This is not surprising as there are only minimal differences visible when inspecting the best-fitting equilibrium and free chemistry models in Fig. 8, and equilibrium chemistry requires a smaller number of free parameters.

In summary, for WASP-94 A b's atmosphere we find subsolar to solar C/O ratios, with the chemical equilibrium values being higher. The inferred atmospheric metallicities are consistent with solar at 1σ–2σ levels, though preferred to be higher, with a range of 1.5–2.4 ± 1.0 × solar when using the equilibrium chemistry results of all reductions at both resolutions. The retrieved C/O ratio and metallicity of our fiducial spectrum (EUREKA! $R = 400$) using our preferred chemical equilibrium model is $\mathrm{C/O} = 0.49^{+0.08}_{-0.13}$ and $Z = 2.17 \pm 0.65$ × solar.

As has been discussed in other works (Welbanks et al. 2019; Reggiani et al. 2022), it is advisable to compare planetary abundances/abundance ratios to those of their specific host star. Teske et al. (2016) focused on the abundances of WASP-94 A relative to WASP-94 B, but here we are interested in just the C/O ratio of WASP-94 A. To derive this value, we use (1) the absolute abundance ranges for oxygen and carbon quoted in Teske et al. (2016) for WASP-94 A from synthesis fitting blended lines (see their section 3.2) as well as (2) previously unreported absolute abundance ranges measured from equivalent width fitting to unblended O I, C I, and CH lines (see Appendix E for more details). Both of these approaches yield consistent results of a $(\mathrm{C/O})_*$ ratio of ∼0.68, using the solar values of carbon and oxygen abundances from Asplund, Amarsi & Grevesse (2021). Encompassing the different carbon and oxygen indicators as well as errors on the stellar parameters, we use a conservative error and proceed with $(\mathrm{C/O})_* = 0.68 \pm 0.10$ for WASP-94 A. This value is in line with what is predicted for a high-metallicity star like WASP-94 A (e.g. Nissen et al. 2014).

Together, these show that the planet's C/O ratio is substellar, at $0.72 \pm 0.17 \times (\mathrm{C/O})_*$. Teske et al. (2016) also measured a precise metallicity for WASP-94 A of 2.09 ± 0.02 × solar (0.32 dex), which is in excellent agreement with our value for WASP-94 A b's atmospheric metallicity of 2.17 ± 0.67 × solar. Thus WASP-94 A b's atmospheric metallicity is $1.04 \pm 0.33 \times (\mathrm{M/H})_*$.

5.1.3 Molecular detections

Using our free chemistry retrievals HYDRA and PRT, we investigate the absorbing molecules present in WASP-94 A b's atmosphere. The constraints of the free chemistry retrieval using HYDRA is shown in Fig. 10. We ran retrievals excluding the individual species for our fiducial spectrum (EUREKA! $R = 400$) and computed the statistical significance via the Bayesian evidence model comparison. The detection significances are summarized in Table 6. The two retrieval set-ups are consistent in their abundance constraints within less than 1σ and we find strong detection significance using HYDRA

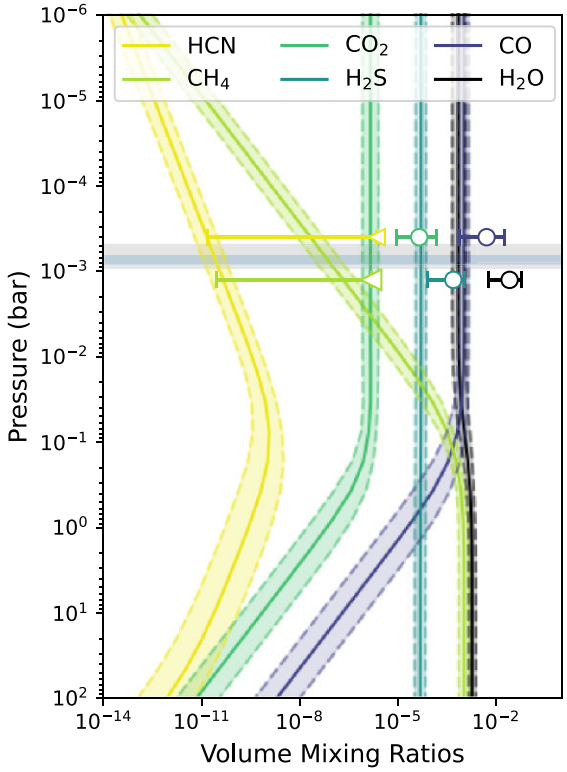

Figure 9. Abundances of the molecules versus pressure in WASP-94 A b's atmosphere as computed by the best-fitting equilibrium chemistry (coloured lines) overlaid with the best-fitting abundances (circles/triangles, 2σ ranges as upper limits for CH_4 and HCH) as determined by the free chemistry model (at arbitrary pressures), both computed with PRT, see also Fig. 8. The reference pressures of the two models are also indicated by the horizontal shaded boxes, with light gray for equilibrium chemistry and darker blue for free chemistry.

and PRT, respectively, for CO_2 ($10.7\sigma, 11.2\sigma$), good detection of H_2O ($4.0\sigma, 4.1\sigma$), and tentative evidence for CO ($2.8\sigma, 3.3\sigma$) and H_2S ($2.9\sigma, 2.1\sigma$).

While we find very strong significance for CO_2 for both retrievals, we only find $\sim 4\sigma$ significance for H_2O for HYDRA. This is in contrast with the high water abundance and therefore significant absorption detected, e.g. see Figs 10, 11 and Table 6. In the case of the HYDRA retrieval, the low detection significance is explained by the fact that the model without H_2O is compensated by very high CO and CO_2 VMRs ($\log(\mathrm{VMR_{CO}}) \gtrsim -2.0$ and $\log(\mathrm{VMR_{CO_2}}) \gtrsim -3$, respectively), and an offset of $\sim$200 ppm. Similarly, PRT finds high mass fractions for CO_2, NH_3, and H_2S, unlikely to be physical, and an offset of $\sim$200 ppm as well. If we fix the offset value to the value found by the base retrieval (93 ppm, Table 4) and redo our retrieval run with and without H_2O, the detection significance increases to 11σ ($\Delta \ln \mathcal{Z} = 59$). Therefore, our quoted 4.1σ can be seen as a lower, conservative detection significance for H_2O driven by the uncertainty in the detector offset. The observations using *JWST* NIRISS/SOSS (GO 5924, PI: Sing) taken in 2024 October will be able to provide additional constraints on the water in the atmosphere of WASP-94 A b, and a combined study will be able to place further constraints on the C/O ratio and atmospheric metallicity. Combining the presented NIRSpec/G395H spectrum with the observations using NIRISS/SOSS may also help to constrain the offset, as we get a better picture of the water abundance and clouds in the atmosphere.

We find tentative evidence for H_2S in the atmosphere of WASP-94 A b. When we retrieve an atmosphere without H_2S with PRT, it compensates for the absence of the molecule by pushing the cloud layer to lower pressures by $\sim$2 mag and decreasing the water abundances, as well as increasing the offset between NRS1 and NRS2. Nevertheless, we find that the model with H_2S in the atmosphere is preferred by a 2.1σ and 2.9σ significance by PRT and HYDRA, respectively. The HYDRA retrievals without H_2S prefer very high CO and CO_2 VMRs of $\log(\mathrm{VMR_{CO}}) \gtrsim -1.5$ and $\log(\mathrm{VMR_{CO_2}}) \gtrsim -3$, with an offset of $\sim$200 ppm. Hence, the model without H_2S is significantly less physically plausible than the model including H_2S, which gives a metallicity of $\sim 41\times$ metallicity for the EUREKA! $R = 400$ data set (see Table 5). We find no evidence for the photochemical product SO_2, which is not expected given WASP-94 A b's equilibrium chemistry and the relatively low metallicity we infer for its atmosphere.

5.2 Implications for planet formation and migration

5.2.1 Inferences from WASP-94's orbital dynamics

The exact formation conditions of WASP-94 A b are hard to deduce, although its highly oblique, retrograde orbit can provide some key clues about its dynamic history. First, the effective temperature of WASP-94 A (6194 ± 5 K; Teske et al. 2016) places the star above the Kraft break (around $\sim$6000 K, dependent on stellar metallicity; Kraft 1967), which delineates the separation between hot, quickly rotating stars and cooler stars with thicker convective envelopes (e.g. Dawson 2014; Albrecht et al. 2022). WASP-94 A b is consistent with the wider observed trend of hot stars hosting hot Jupiters with higher obliquities than cooler stars.

Secondly, the combination of the high obliquity and retrograde nature of WASP-94 A b's orbit can allow us to rule out certain migration pathways. A planet cannot achieve the obliquity of WASP-94 A b by migration through the protoplanetary disc (e.g. Lin & Papaloizou 1986) and so it likely migrated to its close location after disc dispersal. Planet–planet interactions [through scattering or von Zeipel–Kozai–Lidov (vZKL) cycles] would similarly struggle to reach the observed obliquity (Beaugé & Nesvorný 2012; Petrovich & Tremaine 2016). However, vZKL cycles driven by the binary stellar companion could produce the misaligned, and retrograde, orbit of WASP-94 A b (Anderson, Storch & Lai 2016).[1]

The vZKL mechanism (von Zeipel 1910; Kozai 1962; Lidov 1962) suggests that a distant companion can drive alternating cycles of high inclination and eccentricity on the orbit of an inner object and has been widely invoked to explain the close-in orbits of hot Jupiters after subsequent capture by stellar tides (e.g. Holman, Touma & Tremaine 1997; Wu & Murray 2003; Naoz et al. 2011). In particular, Li et al. (2014) describe the eccentric von Zeipel–Kozai–Lidov (EvZKL) mechanism, where a distant stellar companion on an eccentric, coplanar orbit is capable of flipping an inner orbit into a retrograde sense. Their equation (14) presents a compact expression describing the condition for an orbit flip to occur through EvZKL mechanism as a function of orbital eccentricities, through which we hope to place some constraints on the migration history of WASP-94 A b.

We note that this condition is not applicable before disc dispersal; the vZKL mechanism applied to a disc (Martin et al. 2014) leads to a damping of the inclination down to the critical angle of 39° and so would not be capable of flipping the disc. Despite the torque applied by WASP-94 B, disc warping or breaking (e.g. HD 100453; Gonzalez

[1]See fig. 24 of Albrecht et al. (2022) for a comparison of obliquity distributions produced by various dynamic processes.

Table 6. Constrained volume mixing ratios (VMRs) for each molecular species from the best fit, where the uncertainties refer to the 1σ confidence intervals, while the upper limits refer to a 2σ interval. The detection significances for each detected species are shown as computed from the Bayesian evidence values based on the EUREKA! $R = 400$ data set retrievals with HYDRA and PRT.

EUREKA! $R = 400$	HYDRA		PRT	
Species	Log (VMR)	Detection significance (σ)	Log (VMR)	Detection significance (σ)
H_2O	$-1.60^{+0.43}_{-0.40}$	4.0	$-1.59^{+0.35}_{-0.64}$	4.1
CO	$-2.85^{+0.79}_{-5.63}$	2.8	$-2.30^{+0.55}_{-0.84}$	3.3
CO_2	$-4.25^{+0.74}_{-0.54}$	10.7	$-4.35^{+0.52}_{-0.69}$	11.2
CH_4	<-6.29	–	<-5.83	–
NH_3	<-5.10	–	<-5.07	–
HCN	<-5.67	–	<-5.65	–
C_2H_2	<-6.56	–	<-6.23	–
H_2S	$-3.59^{+0.29}_{-0.62}$	2.9	$-3.31^{+0.33}_{-0.80}$	2.1

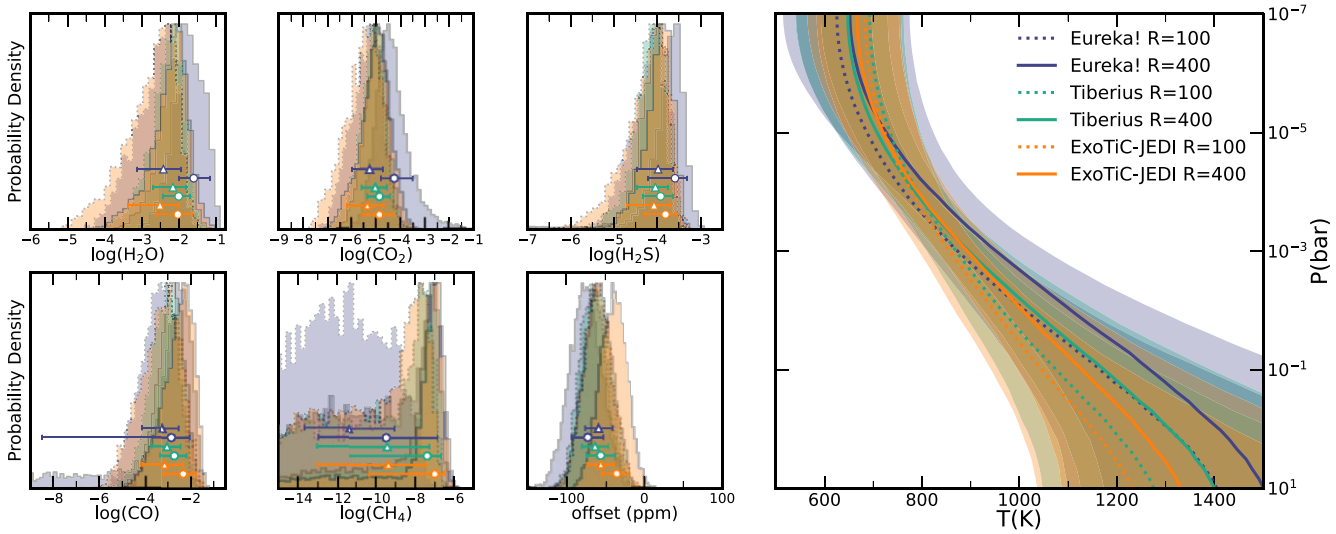

Figure 10. Constrained retrieval parameters for WASP-94 A b from HYDRA for each of the reductions at both binned spectral resolutions. In the left panels, we show the VMRs for the chemical species and the offset (in ppm) between the two detectors. In the right panel, we show the constrained temperature profile, with the median and the $\pm 1\sigma$ range.

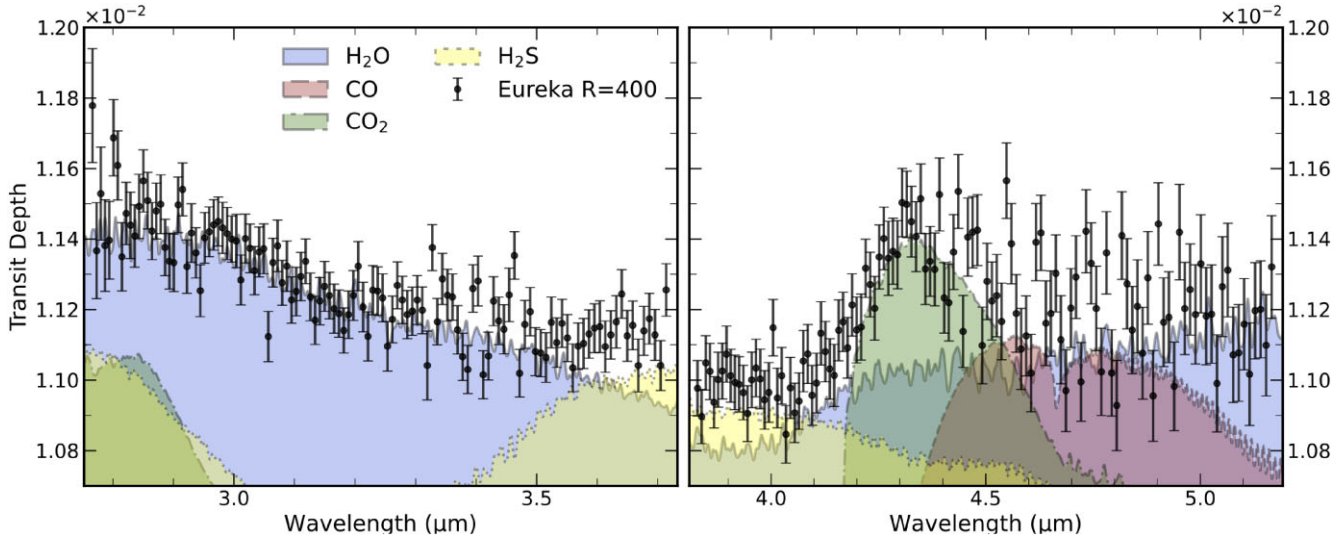

Figure 11. Transmission spectrum of WASP-94 A b using *JWST*'s NIRSpec/G395H with the EUREKA! $R = 400$ data set in black and the best HYDRA fitting retrieval model with each species modelled individually. We show the contribution to the spectrum for the four species that showed a positive detection significance, namely H_2O, CO, CO_2, and H_2S.

et al. 2020; Nealon et al. 2020) is unlikely due to the typically rapid disc communication time-scales in protoplanetary discs (Papaloizou et al. 1995).

The orbit flip condition is highly dependent on the (unknown) eccentricity of the stellar binary orbit and the initial semimajor axis of the planet. Assuming that the currently observed separation between WASP-94 A and WASP-94 B is the semimajor axis of the orbit, the binary orbit would require an eccentricity >0.9 in order to flip a planet orbiting at $a = 10$ au. At a lower eccentricity ($e \sim 0.6$), a planet with $a = 50$ au could plausibly be flipped. For a much more moderate binary eccentricity value of 0.3, the inner planet would need to have formed at hundreds of au from the central star.

The orbits of wide stellar binaries, such as WASP-94, undergo continual evolution under the influence of Galactic tides and stellar flybys (Heggie & Rasio 1996; Jiang & Tremaine 2010; Kaib, Raymond & Duncan 2013) and could achieve the binary eccentricities required in order to flip the orbit of WASP-94 A b. However, without further understanding of the binary orbit's eccentricity and modelling of its evolution, it is hard to place constraints on the formation location of WASP-94 A b other than it likely formed at a large distance from WASP-94 A. With the above conclusions that WASP-94 A b must have undergone high-eccentricity migration driven by the vZKL mechanism after disc dispersal, we would expect to observe a relatively high C/O ratio compared to planets that had migrated through the disc and accreted inner disc material (e.g. Madhusudhan et al. 2014; Booth et al. 2017).

The WASP-94 system architecture may have led to frequent cometary bombardment. Observations of close-in planets coexistent with debris belts reminiscent of the Solar system's Kuiper belt (e.g. Plavchan et al. 2020) suggest that ready reservoirs of pollutant planetesimals may be common in short-period exoplanet systems, even if they are not always observable. Further, observations of near-Sun comets in the Solar system (Jones et al. 2017), and exocomet systems with similar orbital periods to WASP-94 A b (Boyajian et al. 2016; Rappaport et al. 2018; Zieba et al. 2019; Kiefer et al. 2023), show that cometary bodies are capable of reaching hot Jupiter distances. Young & Wyatt (2024) find that the vZKL mechanism can cause an entire planetesimal belt to achieve the extreme eccentricities that would be required to reach the orbital location of WASP-94 A b. Thus, the dynamic processes that caused the peculiar orbit of WASP-94 A b could have also disrupted planetesimal reservoirs and encouraged extremely close forays into the planet's orbital region which may have ended with atmospheric enrichment.

The accretion of cometary material could change the atmospheric C/O ratio and metallicity after the planet has migrated to a close-in location (e.g. AF Lep b; Zhang et al. 2023). Although single cometary impact events, such as the 1994 Shoemaker–Levy 9 Jupiter event, may only impart short-term changes such as brightening events (Nicholson et al. 1995) and atmospheric dispersion of deposited material (Sanchez-Lavega et al. 1998), more sustained bombardment of cometary material may be able to drive larger scale atmospheric changes. Sainsbury-Martinez & Walsh (2024) use a 1D atmospheric model coupled with a parametrized comet impact model to investigate the response of hot Jupiter atmospheres to cometary impacts with approximately the same chemical composition as 67P/Churyumov–Gerasimenko (Le Roy et al. 2015). For an HD 209458 b-like atmosphere with a fiducial C/O ratio of 0.58, Sainsbury-Martinez & Walsh (2024) find that continuous bombardment of the atmosphere by comets could drive the atmospheric C/O down to 0.42–0.48 depending on the mass delivered. However, such a decrease in C/O ratio would also be expected to coincide with an increase in atmospheric metallicity above stellar values, a feature that is not seen in the atmosphere of WASP-94 A b.

5.2.2 Inferences from comparing planetary and stellar C/O and metallicity

WASP-94 A b's substellar atmospheric C/O of $0.49 \pm 0.11 = 0.7 \pm 0.17(\mathrm{C/O})_*$ (based on our fiducial, PRT equilibrium chemistry model using EUREKA! $R = 400$) may provide some clues into its formation history, given its overall metallicity is close to that of the host star. In particular, if one makes the simplest assumption possible for the composition of the solids and gas from which WASP-94 A b formed, i.e. that the total abundances of the species in the disc add up to the star's composition with some species condensed into dust and others left in the gas phase, then it is not possible to reproduce the planet's metallicity and C/O ratio. Instead, a planet formed out of such a reservoir would necessarily have a stellar C/O ratio if it had a stellar metallicity. As a result, the planet must either have accreted solids and gas from different parts of the disc (where the frozen-out species differ) or the disc's composition must have been modified. Accounting for the loss of some species from the WASP-94 A b's atmosphere due to silicate cloud formation would imply that the planet's bulk C/O ratio is lower than the observed atmospheric composition, only worsening the problem (e.g. Calamari et al. 2024).

The difference in C/O ratio between the planet and the star could be explained if the planet accreted its gas far from the host star, where the gas-phase abundances are low (see e.g. Zhang et al. 2021; Bergin et al. 2024). The C/O ratio of the planet would then reflect the composition of the solids accreted, which generally have a substellar C/O between the water snow line (∼1 au) and the location where the last significant carbon carrier disappears from the gas (20–30 au; see e.g. Öberg & Wordsworth 2019). In this scenario, the solids could either be accreted when the planet is still forming if it migrated through the disc,[2] during the phase of high-eccentricity migration responsible for the planet's high obliquity, or even potentially afterwards due to cometary bombardment.

Formation by pebble accretion could also explain WASP-94 A b's C/O and C/H ratios if the enrichment of the inner disc by ices evaporating from the sublimating pebbles is accounted for (e.g. Booth et al. 2017; Booth & Ilee 2019; Schneider & Bitsch 2021). In this scenario, WASP-94 A b would need to have accreted its gaseous envelope in the region where CO_2 or water are released by evaporation from the pebbles (inside ∼5 au), raising the gas-phase C/H abundance back to the stellar value while reducing the C/O ratio. The need for the planet to accrete gas close to its star is, however, difficult to reconcile with the constraints from its orbital obliquity.

Less volatile elements, such as Na or S, can help determine whether pebble accretion or planetesimal/cometary enrichment scenarios are more likely. In particular, the abundances of these species would likely be lower in the pebble accretion scenario because the atmospheric metals would have been accreted predominantly in gaseous form (e.g. Chachan et al. 2023; Crossfield 2023).

[2]However, existing planetesimal accretion models do not readily produce such a population (e.g. Madhusudhan et al. 2014, 2017; Penzlin et al. 2024), because gas accretion is typically assumed to continue throughout the disc's lifetime. These studies assumed stars and discs with a solar composition, but conclusions for abundances normalized to the stellar abundances are relatively insensitive to the assumed composition (e.g. Turrini et al. 2021).

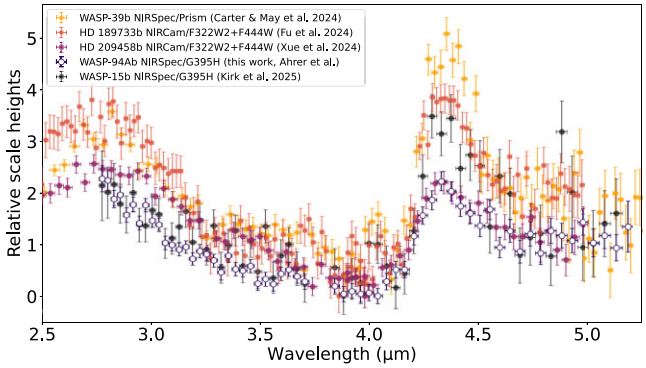

Figure 12. WASP-94 A b in context with *JWST* transmission spectra published for hot Jupiters (here assumed as exoplanets with temperatures 1000–2000 K, radii $R_p > 0.5\,R_{Jup}$, and masses $M_p > 0.2\,M_{Jup}$) in the 2.5–5.2 μm wavelength range: WASP-39 b (Carter et al. 2024), HD 189733b (Fu et al. 2024), HD 209458b (Xue et al. 2024), and WASP-15 b (Kirk et al. 2025). The colours represent the order of temperatures, from light to dark: WASP-39 b (∼1170 K), HD 189733b (∼1200 K), HD 209458b (∼1460 K), WASP-94 A b (∼1500 K; best-fitting offset applied), and WASP-15 b (∼1680 K). The scale heights are computed using a mean molecular mass of $\mu = 2.3$ amu and normalized using the minimum of the transit depth.

We assess the possibility of using volatile elements to constrain pebble accretion versus planetesimal/cometary accretion by comparing the measured sodium abundances between the star and the planet. WASP-94 A's sodium abundance is Na/H $= 2.63 \pm 0.25\times$ solar (Teske et al. 2016), assuming a sodium solar abundance from Asplund et al. (2009) of $\log_{10}$ Na $= 6.24 \pm 0.04$ sodium atoms for 10^{12} hydrogen atoms. We compute WASP-94 A b's abundance of sodium relative to hydrogen, Na/H, using the measured VMR of Na in WASP-94 A b's atmosphere from Ahrer et al. (2024) and the hydrogen in the atmosphere calculated by our best-fitting equilibrium chemistry model. Following Welbanks et al. (2019) we find Na/H $= 0.079^{+3.1}_{-0.072}\times$ solar for WASP-94 A b. Note that this is a lower limit, as the VMR of Na is relatively unconstrained, and the sodium has been retrieved separately from the abundance of hydrogen. So WASP-94 A b's Na abundance can be estimated as substellar to stellar at $0.030^{+1.2}_{-0.028}$ times the Na abundance of its host star (likely a lower limit). This suggests a (very) slight preference for the pure pebble accretion scenario which would cause a very low Na/H compared to the star, however, a planetesimal scenario is equally likely as this would allow a stellar to superstellar Na/H. Further constraints on the Na abundance are needed e.g. by gathering more high-resolution observations and modelling them together with the low-resolution spectrum to get a tighter constraint on the Na abundance.

Altogether, the orbital obliquity, C/O ratio, metallicity, and Na/H abundance hint at a planet that formed far from its star before reaching its current location by high-eccentricity migration, with WASP-94 A b acquiring its volatiles from planetesimals accreted along the way or subsequent bombardment from outer disc material.

5.3 *JWST* transmission spectra of hot Jupiters

Only a small sample of hot Jupiters (temperatures 1000–2000 K, radii $R_p > 0.5\,R_{Jup}$, and masses $M_p > 0.2\,M_{Jup}$) have published *JWST* transmission spectra thus far. In Fig. 12, we compare WASP-94 A b's transmission spectrum with the four other hot Jupiters for which spectra in the wavelength range of 2.5–5.2 μm were available. The coolest planet of the sample, WASP-39 b (Carter et al. 2024), shows the largest CO_2 absorption feature in atmospheric scale heights in addition to a strong H_2O and the SO_2 feature (∼4 μm). The second coolest planet, HD 189733b, shows similarly large features, though excluding the SO_2 absorption (Fu et al. 2024). The hottest out of the sample, WASP-15 b (Kirk et al. 2025), also shows a large CO_2 bump and a tentative SO_2 detection. This trend also follows the description that higher atmospheric metallicity is needed to produce the photochemical product SO_2. By eye, WASP-94 A b is most similar to HD 209458b (Xue et al. 2024), in terms of CO_2, lack of detection of SO_2, and in temperature, though WASP-94 A b's H_2O slope is potentially less steep.

6 CONCLUSIONS

We presented *JWST* NIRSpec/G395H transit spectroscopy observations of WASP-94 A b, a hot Jupiter in a retrograde and misaligned orbit around its F-type host star. We used three independent pipelines to determine the planet's transmission spectrum. We also probed for limb asymmetries, but while the morning and evening spectra do appear to show evidence for differences, it is not statistically favoured over a uniform limb approach.

WASP-94 A b's transmission spectrum shows strong H_2O and CO_2 absorption bands with detection significances of 4σ and 11σ from both our retrievals, PRT and HYDRA. The former relatively low detection significance is likely due to the fact that the full water feature is not covered within G395H's wavelength range (see e.g. the comparison to HD 209458b's spectrum in Fig. 12). When excluding H_2O both our retrieval set-ups retrieved high offsets between the NRS1 and NRS2 detectors (190 ppm) and very high CO_2 abundance to account for the non-presence of H_2O in the model but still managed to get comparatively statistically valid fit. When fixing the detector offset to the value found by the base retrieval, we find higher detection significance for H_2O at $\sim 11\sigma$, concluding that the driving factor is the uncertainty in the detector offset. We further find tentative evidence for CO (HYDRA: 2.8σ; PRT: 3.3σ) and H_2S (HYDRA: 2.9σ; PRT: 2.1σ) using our independent retrieval set-ups.

We include an offset between the two NIRSpec/G395H detectors NRS1 and NRS2 in our retrieval analysis (Table 4) as our reductions show slight offsets in the NRS1 detector and are also preferred based on the larger Bayesian evidence values. We caution the community for future NIRSpec/G395H studies as we find that the inclusion of an offset may significantly change the detection significances for some of the molecules, as well as influence the C/O ratio inferred by equilibrium chemistry. A larger sample size (with a range of number of groups/integration) of hot Jupiter observations with NIRSpec/G395H and further investigation by the community is needed to achieve an accurate picture of whether an offset is necessary to be included between NRS1 and NRS2 for all observations and how large it can realistically be.

Using our best-fitting equilibrium chemistry to our fiducial data set (EUREKA! $R = 400$), we derive a C/O ratio for WASP-94 A b's atmosphere of $0.49^{+0.08}_{-0.13}$, which is consistent within the uncertainties with the derived C/O for the two other independent data reductions, and at both resolutions we computed for this analysis ($R = 100$ and 400). Similarly consistent is our retrieved atmospheric metallicity of $2.17 \pm 0.65\times$ solar. While WASP-94 A b's metallicity is in line with the stellar metallicity ($2.09 \pm 0.02\times$ solar), the planet's C/O ratio is $0.70 \pm 0.17\times$ the star's C/O ratio.

Formation by pebble accretion is one mechanism that would naturally explain WASP-94 A b's composition, assuming evaporation

from pebbles in the inner disc, i.e. CO_2 or water is released to the gas and therefore reducing its C/O ratio. Other possibilities include planetesimal accretion in combination with large-distance migration or accretion of solids and gas from different parts of the disc. We find that this lower C/O ratio is unlikely to be caused by the accretion of cometary impact events. While this can decrease the atmospheric C/O, it would also increase the atmospheric metallicity, which is not the case for WASP-94 A b. Note that there is the caveat that silicate clouds likely form in WASP-94 A b's atmosphere, which we are not sensitive to using NIRSpec/G395H. This could further affect the measured C/O ratio.

Further observations of WASP-94 A b are necessary to achieve tighter constraints on the molecular abundances and clouds within its atmosphere, which in turn allows better constrained C/O ratio and metallicity measurements. In addition, in order to rule out possible formation scenarios for WASP-94 A b, we require additional elemental abundances, e.g. those of refractory species. Using the Na abundance reported for WASP-94 A b in the literature, we find a substellar to stellar Na/H which can be explained by both pebble and planetesimal accretion.

Our observations showed that WASP-94 A b is one of the most favourable targets for transmission spectroscopy as its large scale height and the brightness of the star result in uncertainties per scale height comparable to HD 209458 b (see Fig. 12). With our observations, we placed meaningful constraints on the C/O ratio and metallicity of WASP-94 A b based on the molecular detections using *JWST* NIRSpec/G395H. This points the way to an even more complete characterization and stronger constraints on formation and evolution with complementary data sets.

ACKNOWLEDGEMENTS

This work is based on observations made with the NASA/ESA/CSA *JWST*. The data were obtained from the *Mikulski Archive for Space Telescopes* at the Space Telescope Science Institute, which is operated by the Association of Universities for Research in Astronomy, Inc., under NASA contract NAS 5-03127 for *JWST*. These observations are associated with program #3154. E-MA is grateful to L. Welbanks for providing details about the Na/H calculations following Welbanks et al. (2019) and P. Mollière for PRT support. JK acknowledges financial support from Imperial College London through an Imperial College Research Fellowship grant. Support for program #3154 was provided to JT by NASA through a grant from the Space Telescope Science Institute, which is operated by the Association of Universities for Research in Astronomy, Inc., under NASA contract NAS5-03127. CHM gratefully acknowledges the Leverhulme Centre for Life in the Universe at the University of Cambridge for support through the Joint Collaborations Research Project Grant GAG/382. RN acknowledges funding from the UK Research and Innovation (UKRI)/Engineering and Physical Sciences Research Council (EPSRC) through a Stephen Hawking Fellowship (EP/T017287/1). PJW acknowledges support from the Science and Technology Facilities Council (STFC) through consolidated grant ST/X001121/1. MZ acknowledges support from a UKRI Future Leaders Fellowship (Grant MR/T040866/1), a STFC Funding Nucleus Award (Grant ST/T000082/1), and the Leverhulme Trust through a research project grant (RPG-2020-82). VP acknowledges support from the UKRI Future Leaders Fellowship grants (MR/S035214/1 and MR/Y011759/1) and UKRI STFC through the consolidated grant ST/X001121/1.

We thank the anonymous referee for their time and valuable feedback which improved the paper.

DATA AVAILABILITY

The data products (light curves, transmission spectra, and retrieval products) associated with this paper are available via Zenodo at https://doi.org/10.5281/zenodo.15430203. The data from JWST program #3154 described here may be obtained from http://dx.doi.org/10.17909/gsq8-zc73.

REFERENCES

Ahrer E., Wheatley P. J., Kirk J., Gandhi S., King G. W., Louden T., 2022, MNRAS, 510, 4857
Ahrer E. M. et al., 2023, Nature, 614, 653
Ahrer E. et al., 2024, MNRAS, 530, 2749
Albrecht S. et al., 2012, ApJ, 757, 18
Albrecht S. H., Dawson R. I., Winn J. N., 2022, PASP, 134, 082001
Alderson L., Grant D., Wakeford H., 2022, Exo-TiC/ExoTiC-JEDI: v0.1-beta-release. Zenodo, available at: https://zenodo.org/records/7185855
Alderson L. et al., 2023, Nature, 614, 664
Alderson L. et al., 2024, AJ, 167, 216
Alderson L. et al., 2025, AJ, 169, 142
Anderson K. R., Storch N. I., Lai D., 2016, MNRAS, 456, 3671
Andrae R. et al., 2023, A&A, 674, A27
Asplund M., Grevesse N., Sauval A. J., Scott P., 2009, ARA&A, 47, 481
Asplund M., Amarsi A. M., Grevesse N., 2021, A&A, 653, A141
Azzam A. A., Tennyson J., Yurchenko S. N., Naumenko O. V., 2016, MNRAS, 460, 4063
Barber R. J., Strange J. K., Hill C., Polyansky O. L., Mellau G. C., Yurchenko S. N., Tennyson J., 2014, MNRAS, 437, 1828
Beaugé C., Nesvorný D., 2012, ApJ, 751, 119
Bell T. J. et al., 2022, J. Open Source Softw., 7, 4503
Bell T. J. et al., 2023a, preprint (arXiv:2301.06350)
Bell T. J. et al., 2023b, Nature, 623, 709
Bello-Arufe A. et al., 2025, ApJ, 980, L26
Bergin E. A., Booth R. A., Colmenares M. J., Ilee J. D., 2024, ApJ, 969, L21
Bonomo A. S. et al., 2017, A&A, 602, A107
Booth R. A., Ilee J. D., 2019, MNRAS, 487, 3998
Booth R. A., Clarke C. J., Madhusudhan N., Ilee J. D., 2017, MNRAS, 469, 3994
Boss A. P., 1997, Science, 276, 1836
Boyajian T. S. et al., 2016, MNRAS, 457, 3988
Buchner J. et al., 2014, A&A, 564, A125
Bushouse H. et al., 2024, *JWST* Calibration Pipeline (1.14.0). Zenodo, available at: https://zenodo.org/records/10870758
Calamari E., Faherty J. K., Visscher C., Gemma M. E., Burningham B., Rothermich A., 2024, ApJ, 963, 67
Carter A. L. et al., 2024, Nat. Astron., 8, 1008
Chachan Y., Knutson H. A., Lothringer J., Blake G. A., 2023, ApJ, 943, 112
Charbonneau D., Brown T. M., Noyes R. W., Gilliland R. L., 2002, ApJ, 568, 377
Chubb K. L. et al., 2018, J. Quant. Spectrosc. Radiat. Transf., 218, 178
Chubb K. L., Tennyson J., Yurchenko S. N., 2020, MNRAS, 493, 1531
Claret A., 2000, A&A, 363, 1081
Coles P. A., Yurchenko S. N., Tennyson J., 2019, MNRAS, 490, 4638
Crossfield I. J. M., 2023, ApJ, 952, L18
Dawson R. I., 2014, ApJ, 790, L31
Dawson R. I., Johnson J. A., 2018, ARA&A, 56, 175
Esparza-Borges E. et al., 2023, ApJ, 955, L19
Espinoza N., Jones K., 2021, AJ, 162, 165
Espinoza N. et al., 2024, Nature, 632, 1017
Fabrycky D. C., Winn J. N., 2009, ApJ, 696, 1230
Feinstein A. D. et al., 2023, Nature, 614, 670
Feroz F., Hobson M. P., 2008, MNRAS, 384, 449
Feroz F., Hobson M. P., 2013, MNRAS, 437, 3540
Feroz F., Hobson M. P., Bridges M., 2009, MNRAS, 398, 1601
Foreman-Mackey D., Hogg D. W., Lang D., Goodman J., 2013, PASP, 125, 306

Fu G. et al., 2024, Nature, 632, 752
Gaia Collaboration, 2023, A&A, 674, A1
Gandhi S., Madhusudhan N., Hawker G., Piette A., 2019, AJ, 158, 228
Gandhi S., Kesseli A., Snellen I., Brogi M., Wardenier J. P., Parmentier V., Welbanks L., Savel A. B., 2022, MNRAS, 515, 749
Garhart E. et al., 2020, AJ, 159, 137
Goldreich P., Tremaine S., 1980, ApJ, 241, 425
Gonzalez J.-F. et al., 2020, MNRAS, 499, 3837
Grant D., Wakeford H. R., 2024, J. Open Source Softw., 9, 6816
Grant D. et al., 2023a, ApJ, 949, L15
Grant D. et al., 2023b, ApJ, 956, L32
Harris G. J., Tennyson J., Kaminsky B. M., Pavlenko Y. V., Jones H. R. A., 2006, MNRAS, 367, 400
Heggie D. C., Rasio F. A., 1996, MNRAS, 282, 1064
Høg E. et al., 2000, A&A, 363, 385
Holman M., Touma J., Tremaine S., 1997, Nature, 386, 254
Inglis J. et al., 2024, ApJ, 973, L41
Jeffreys H., 1983, Theory of Probability. Clarendon Press, Oxford
Jiang Y.-F., Tremaine S., 2010, MNRAS, 401, 977
Jones K., Espinoza N., 2020, J. Open Source Softw., 5, 2382
Jones G. H. et al., 2017, Space Sci. Rev., 214, 20
JWST Transiting Exoplanet Community Early Release Science Team, 2023, Nature, 614, 649
Kaib N. A., Raymond S. N., Duncan M., 2013, Nature, 493, 381
Kiefer F. et al., 2023, A&A, 671, A25
Kirk J., Wheatley P. J., Louden T., Doyle A. P., Skillen I., McCormac J., Irwin P. G. J., Karjalainen R., 2017, MNRAS, 468, 3907
Kirk J. et al., 2021, AJ, 162, 34
Kirk J. et al., 2024a, RAS Tech. Instrum., 3, 691
Kirk J. et al., 2024b, AJ, 167, 90
Kirk J. et al., 2025, MNRAS, 537, 3027
Kokori A. et al., 2023, ApJS, 265, 4
Kozai Y., 1962, AJ, 67, 591
Kraft R. P., 1967, ApJ, 150, 551
Kreidberg L., 2015, PASP, 127, 1161
Le Roy L. et al., 2015, A&A, 583, A1
Li G., Naoz S., Kocsis B., Loeb A., 2014, ApJ, 785, 116
Lidov M. L., 1962, Planet. Space Sci., 9, 719
Lin D. N. C., Papaloizou J., 1986, ApJ, 309, 846
Lin D. N., Bodenheimer P., Richardson D. C., 1996, Nature, 380, 606
Louie D. R. et al., 2025, AJ, 169, 86
MacDonald R. J., Goyal J. M., Lewis N. K., 2020, ApJ, 893, L43
Madhusudhan N., Seager S., 2009, ApJ, 707, 24
Madhusudhan N., Amin M. A., Kennedy G. M., 2014, ApJ, 794, 12
Madhusudhan N., Bitsch B., Johansen A., Eriksson L., 2017, MNRAS, 469, 4102
Magic Z., Chiavassa A., Collet R., Asplund M., 2015, A&A, 573, A90
Martin R. G., Nixon C., Lubow S. H., Armitage P. J., Price D. J., Doğan S., King A., 2014, ApJ, 792, L33
May E. M. et al., 2023, ApJL, 959, L9
Mayor M. et al., 2003, The Messenger, 114, 20
Meech A. et al., 2025, MNRAS, 539, 1381
Mollière P., Wardenier J. P., Van Boekel R., Henning T., Molaverdikhani K., Snellen I. A., 2019, A&A, 627, A67
Moran S. E. et al., 2023, ApJ, 948, L11
Murphy M. M. et al., 2024, Nat. Astron., 8, 1562
Naoz S., Farr W. M., Lithwick Y., Rasio F. A., Teyssandier J., 2011, Nature, 473, 187
Nasedkin E., Mollière P., Blain D., 2024, J. Open Source Softw., 9, 5875
Nealon R., Cuello N., Gonzalez J.-F., van der Plas G., Pinte C., Alexander R., Ménard F., Price D. J., 2020, MNRAS, 499, 3857
Neveu-Vanmalle M. et al., 2014, A&A, 572, A49
Nicholson P. D. et al., 1995, Geophys. Res. Lett., 22, 1613
Nissen P. E., Chen Y. Q., Carigi L., Schuster W. J., Zhao G., 2014, A&A, 568, A25
Notsu S., Eistrup C., Walsh C., Nomura H., 2020, MNRAS, 499, 2229
Öberg K. I., Wordsworth R., 2019, AJ, 158, 194
Öberg K. I., Murray-Clay R., Bergin E. A., 2011, ApJ, 743, 16
Ohno K. et al., 2025, ApJL, 979, L7
Papaloizou J. C. B., Lin D. N. C., Papaloizou J. C. B., Lin D. N. C., 1995, ApJ, 438, 841
Penzlin A. B. T. et al., 2024, MNRAS, 535, 171
Petrovich C., Tremaine S., 2016, ApJ, 829, 132
Plavchan P. et al., 2020, Nature, 582, 497
Pollacco D. et al., 2006, PASP, 118, 1407
Pollack J. B. et al., 1996, Icarus, 124, 62
Polyansky O. L., Kyuberis A. A., Zobov N. F., Tennyson J., Yurchenko S. N., Lodi L., 2018, MNRAS, 480, 2597
Pont F., Zucker S., Queloz D., 2006, MNRAS, 373, 231
Radica M. et al., 2023, MNRAS, 524, 835
Rafikov R. R., 2005, ApJ, 621, L69
Rafikov R. R., 2006, ApJ, 648, 666
Ramírez I., Allende Prieto C., Lambert D. L., 2007, A&A, 465, 271
Ramírez I., Meléndez J., Asplund M., 2014, A&A, 561, A7
Rappaport S. et al., 2018, MNRAS, 474, 1453
Rasio F. A., Ford E. B., Rasio F. A., Ford E. B., 1996, Science, 274, 954
Reggiani H., Schlaufman K. C., Healy B. F., Lothringer J. D., Sing D. K., 2022, AJ, 163, 159
Richard C. et al., 2012, J. Quant. Spectrosc. Radiat. Transf., 113, 1276
Rothman L. S. et al., 2010, J. Quant. Spectrosc. Radiat. Transf., 111, 2139
Rustamkulov Z. et al., 2023, Nature, 614, 659
Sainsbury-Martinez F., Walsh C., 2024, ApJ, 966, 39
Sanchez-Lavega A., Gómez J. M., Rojas J. F., Acarreta J. R., Lecacheux J., Colas F., Hueso R., Arregui J., 1998, Icarus, 131, 341
Schmidt S. P. et al., 2025, preprint (arXiv:2501.18477)
Schneider A. D., Bitsch B., 2021, A&A, 654, A71
Skrutskie M. F. et al., 2006, AJ, 131, 1163
Speagle J. S., 2020, MNRAS, 493, 3132
Stassun K. G., Collins K. A., Gaudi B. S., 2017, AJ, 153, 136
Taylor J. et al., 2023, MNRAS, 524, 817
Teske J. K., Khanal S., Ramírez I., 2016, ApJ, 819, 19
Trotta R., 2008, Contemp. Phys., 49, 71
Tsai S. M. et al., 2023, Nature, 617, 483
Turrini D. et al., 2021, ApJ, 909, 40
Virtanen P. et al., 2020, Nat. Methods, 17, 261
von Zeipel H., 1910, Astron. Nachr., 183, 345
Wakeford H., Grant D., 2022, Exo-TiC/ExoTiC-LD: ExoTiC-LD v2.1 Zenodo Release (v2.1.0). Zenodo, available at: https://zenodo.org/records/6809899
Weidenschilling S. J., Marzari F., Weidenschilling S. J., Marzari F., 1996, Nature, 384, 619
Welbanks L., Madhusudhan N., 2021, ApJ, 913, 114
Welbanks L., Madhusudhan N., 2022, ApJ, 933, 79
Welbanks L., Madhusudhan N., Allard N. F., Hubeny I., Spiegelman F., Leininger T., 2019, ApJ, 887, L20
Wu Y., Murray N., 2003, ApJ, 589, 605
Xue Q., Bean J. L., Zhang M., Welbanks L., Lunine J., August P., 2024, ApJ, 963, L5
Young S. D., Wyatt M. C., 2024, MNRAS, 527, 5244
Yurchenko S. N., Mellor T. M., Freedman R. S., Tennyson J., 2020, MNRAS, 496, 5282
Zanazzi J. J., Dewberry J., Chiang E., 2024, ApJ, 967, L29
Zhang K. et al., 2021, ApJS, 257, 5
Zhang Z. et al., 2023, AJ, 166, 198
Zieba S., Zwintz K., Kenworthy M. A., Kennedy G. M., 2019, A&A, 625, L13

APPENDIX A: ASYMMETRIC LIMB STUDY FOR ALL REDUCTIONS WITH CATWOMAN

Following the result from applying an asymmetric transit model using CATWOMAN (Jones & Espinoza 2020; Espinoza & Jones 2021) to the EUREKA! $R = 100$ light curves in Section 3.3.2, we demonstrate here that with the same set-up applied to the $R = 100$ light curves from the EXOTIC-JEDI and TIBERIUS reductions, we obtain consistent

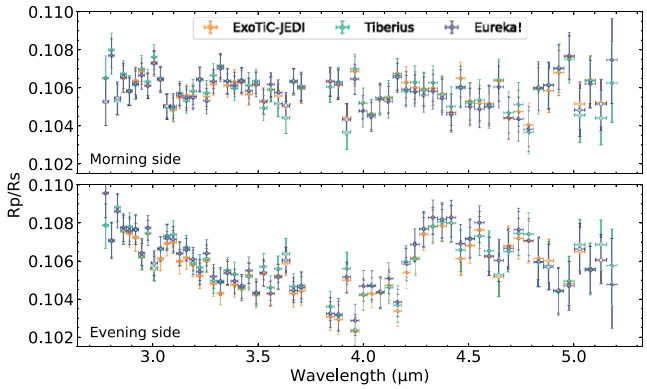

Figure A1. Morning (top) and evening (bottom) transmission spectra of WASP-94 A b using the $R = 100$ light curves for the three independent reductions: EUREKA!, TIBERIUS, and EXOTIC-JEDI.

results, see Fig. A1. For all reductions and light curves, the difference in Bayesian evidence between the simple transit model and the asymmetric model is not statistically significant with differences in Bayesian evidences $\Delta \ln \mathcal{Z} < 1.5$.

APPENDIX B: RETRIEVAL PRIOR RANGES

Here we provide tables with the prior ranges of our retrieval set-ups, HYDRA and PRT (Table B1) and the references for the line lists used in our retrievals.

Table B1. Parameters and uniform prior ranges for our retrieval of WASP-94 A b with HYDRA (top) and PRT equilibrium and free chemistry retrievals (bottom; chemical set-up is highlighted in bold). Note that they are all uniform except the planetary mass parameter. The rightmost column refers to the literature references of the species as follows: [1] Polyansky et al. (2018); [2] Rothman et al. (2010); [3] Coles, Yurchenko & Tennyson (2019); [4] Harris et al. (2006); Barber et al. (2014); [5] Chubb, Tennyson & Yurchenko (2020); [6] Azzam et al. (2016); Chubb et al. (2018); and [7] Yurchenko et al. (2020).

	Parameter	Prior range	Reference
	HYDRA		
Free chemistry (VMR)	$\log(H_2O)$	$-15 \rightarrow -0$	[1]
	$\log(CO)$	$-15 \rightarrow -1$	[2]
	$\log(CO_2)$	$-15 \rightarrow -1$	[2]
	$\log(CH_4)$	$-15 \rightarrow -1$	[2]
	$\log(NH_3)$	$-15 \rightarrow -1$	[3]
	$\log(HCN)$	$-15 \rightarrow -1$	[4]
	$\log(C_2H_2)$	$-15 \rightarrow -1$	[5]
	$\log(H_2S)$	$-15 \rightarrow -1$	[6]
Temp. profile	$T_{1\mathrm{mbar}}$ (K)	$300 \rightarrow 2500$	
	α_1 (K)	$0 \rightarrow 1$	
	α_2 (K)	$0 \rightarrow 1$	
	$\log(P_1)$ (bar)	$-6 \rightarrow 2$	
	$\log(P_2)$ (bar)	$-6 \rightarrow 2$	
	$\log(P_3)$ (bar)	$-2 \rightarrow 2$	
Ref. pressure	$\log(P_{\mathrm{ref}})$ (bar)	$-6 \rightarrow 2$	
Clouds/hazes	$\log(\alpha_{\mathrm{haze}})$	$-4 \rightarrow 6$	
	γ_{haze}	$-20 \rightarrow -1$	
	$\log(P_{\mathrm{cl}})$ (bar)	$-6 \rightarrow 2$	
	ϕ_{cl}	$0 \rightarrow 1$	
Offset	Δ_{1-2} (ppm)	$-200 \rightarrow 200$	
	PETITRADTRANS (PRT)		
Equilibrium chemistry	C/O	$0.1 \rightarrow 1.5$	
	$\log(Fe/H)$	$-3 \rightarrow 2$	
Free chemistry (mass fractions)	$\log(H_2O)$	$-10 \rightarrow -1e\text{-}6$	[2]
	$\log(CO_2)$	$-10 \rightarrow -1e\text{-}6$	[7]
	$\log(CO)$	$-10 \rightarrow -1e\text{-}6$	[2]
	$\log(CH_4)$	$-10 \rightarrow -1e\text{-}6$	[2]
	$\log(NH_3)$	$-10 \rightarrow -1e\text{-}6$	[3]
	$\log(HCN)$	$-10 \rightarrow -1e\text{-}6$	[4]
	$\log(C_2H_2)$	$-10 \rightarrow -1e\text{-}6$	[5]
	$\log(H_2S)$	$-10 \rightarrow -1e\text{-}6$	[6]
Temp. profile	T (K)	$500 \rightarrow 2500$	
Ref. pressure	$\log(P_{\mathrm{ref}})$ (bar)	$-6 \rightarrow -2$	
Planet mass	M_{p} (M_{Jup})	$\mathcal{N}(\mu = 0.456,\ \sigma = 0.05)$	
Clouds	$\log(P_{\mathrm{cloud}})$ (bar)	$-8 \rightarrow 2$	
Offset	Offset (ppm)	$-200 \rightarrow 200$	

APPENDIX C: COMPREHENSIVE RETRIEVAL RESULTS

Table C1 shows the retrieval results of all PRT and HYDRA runs of all three reductions at both computed resolutions ($R = 100$ and $R = 400$).

Table C1. Atmospheric retrieval results, with 1σ uncertainties, except in the case of unconstrained parameters.

Input spectrum	$\ln \mathcal{Z}$	Mass	$T_{\rm ref}$ [a] (K)	$P_{\rm ref}$ (bar)	$\log \alpha_{\rm haze}$	$\gamma_{\rm haze}$	$\log P_{\rm cloud}$ (bar)	$\phi_{\rm cl}$
EUREKA! $R = 400$								
PRT: equilibrium chemistry	1875.1 ± 0.1	0.472 ± 0.049	955 ± 44	-3.15 ± 0.31	–	–	-2.60 ± 0.23	–
PRT: free chemistry	1871.4 ± 0.1	0.474 ± 0.048	702 ± 82	-3.34 ± 0.43	–	–	-0.5 ± 1.6	–
HYDRA: free chemistry	1872.4 ± 0.1	–	814 ± 76	-3.58 ± 0.35	0.94 ± 3.00	-11 ± 6	-0.8 ± 1.8	0.44 ± 0.32
TIBERIUS $R = 400$								
PRT: equilibrium chemistry	1928.1 ± 0.1	0.464 ± 0.039	948 ± 29	-3.05 ± 0.16	–	–	-2.33 ± 0.13	–
PRT: free chemistry	1925.3 ± 0.1	0.469 ± 0.043	648 ± 61	-3.01 ± 0.38	–	–	0.1 ± 1.4	–
HYDRA: free chemistry	1924.5 ± 0.1	–	772 ± 59	-3.20 ± 0.28	0.75 ± 3.09	-11 ± 6	-0.6 ± 1.6	0.43 ± 0.32
EXOTIC-JEDI $R = 400$								
PRT: equilibrium chemistry	1792.8 ± 0.1	0.467 ± 0.038	973 ± 27	-3.11 ± 0.15	–	–	-2.31 ± 0.13	–
PRT: free chemistry	1788.4 ± 0.1	0.482 ± 0.045	753 ± 84	-3.49 ± 0.52	–	–	0.1 ± 1.3	–
HYDRA: free chemistry	1790.5 ± 0.1	–	828 ± 66	-3.41 ± 0.37	0.72 ± 3.03	-11 ± 6	-0.5 ± 1.6	0.44 ± 0.31
EUREKA! $R = 100$								
PRT: equilibrium chemistry	514.5 ± 0.1	0.476 ± 0.049	984 ± 44	-3.25 ± 0.33	–	–	-2.61 ± 0.24	–
PRT: free chemistry	511.8 ± 0.1	0.476 ± 0.046	686 ± 58	-3.18 ± 0.47	–	–	0.0 ± 1.4	–
HYDRA: free chemistry	516.1 ± 0.1	–	779 ± 51	-2.98 ± 0.41	0.56 ± 3.12	-11 ± 6	-0.4 ± 1.5	0.45 ± 0.33
TIBERIUS $R = 100$								
PRT: equilibrium chemistry	518.0 ± 0.1	0.462 ± 0.045	939 ± 33	-3.09 ± 0.21	–	–	-2.36 ± 0.20	–
PRT: free chemistry	516.4 ± 0.1	0.461 ± 0.043	635 ± 60	-2.94 ± 0.39	–	–	-0.3 ± 1.5	–
HYDRA: free chemistry	518.1 ± 0.1	–	745 ± 52	-3.05 ± 0.33	0.77 ± 3.08	-11 ± 6	-0.5 ± 1.5	0.45 ± 0.32
EXOTIC-JEDI $R = 100$								
PRT: equilibrium chemistry	480.5 ± 0.1	0.462 ± 0.045	973 ± 30	-3.14 ± 0.21	–	–	-2.35 ± 0.19	–
PRT: free chemistry	477.5 ± 0.1	0.472 ± 0.041	675 ± 63	-3.09 ± 0.48	–	–	0.2 ± 1.3	–
HYDRA: free chemistry	480.7 ± 0.1	–	753 ± 55	-2.75 ± 0.45	0.75 ± 3.11	-11 ± 6	-0.3 ± 1.5	0.44 ± 0.32

[a] $T_{\rm ref}$ corresponds to the temperature of the isothermal temperature profile in the case of PRT and to the temperature at 1 mbar in the case of HYDRA. The corresponding detector offsets for these retrievals can be found in Table 4.

APPENDIX D: CORNER PLOTS

Here we include the posterior plots for the PRT equilibrium chemistry retrieval runs for all reductions in Fig. D1 at $R = 400$, as well as the posterior of the free chemistry HYDRA retrieval of WASP-94 A b using the EUREKA! $R = 400$ data set in Fig. D2.

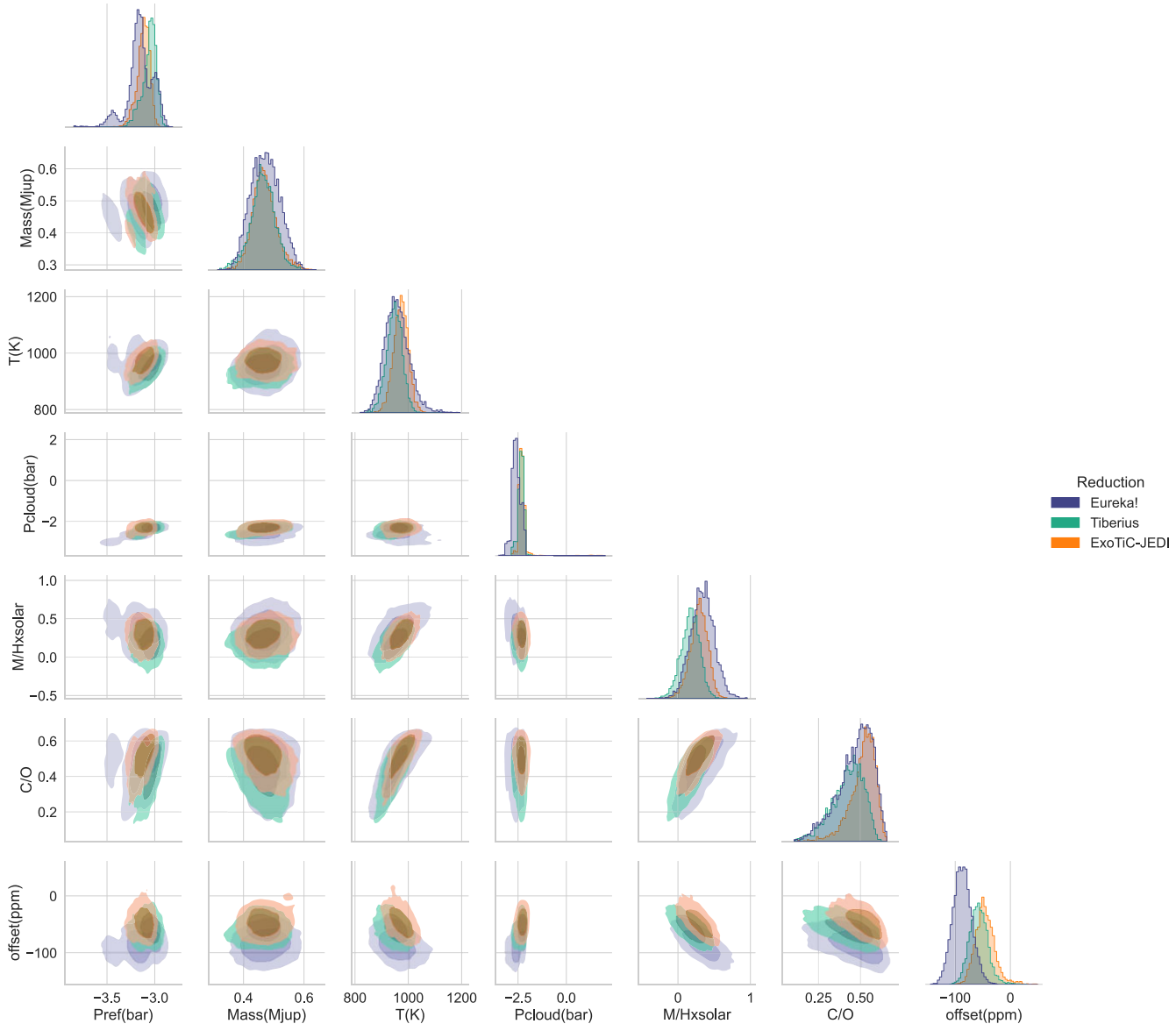

Figure D1. Posterior plots of the PRT equilibrium chemistry runs for EUREKA!, TIBERIUS, and EXOTIC-JEDI at $R = 400$. The two shadings correspond to the 1σ (darker) and 2σ (lighter) confidence intervals.

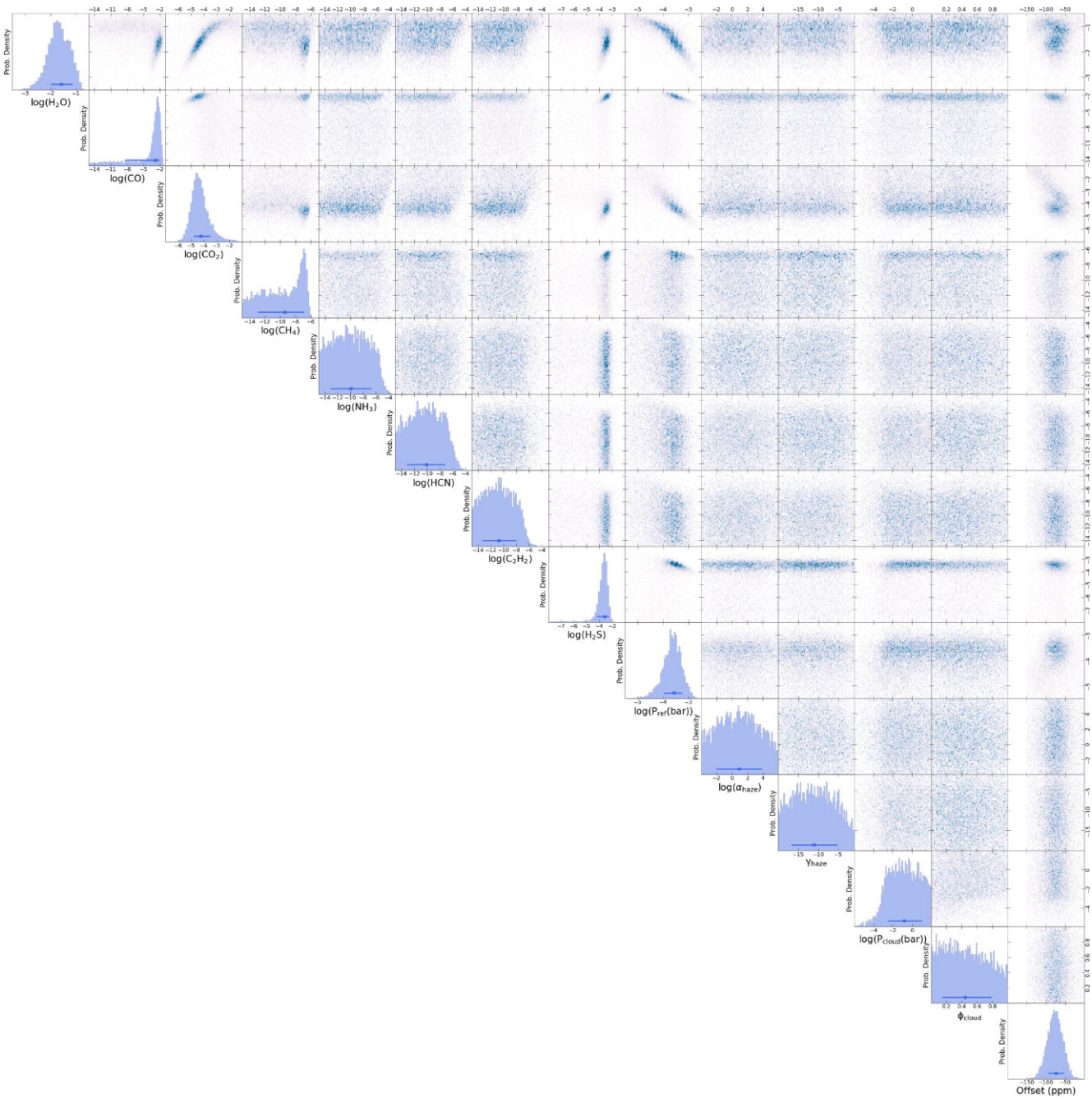

Figure D2. Posterior of the retrieval of WASP-94 A b using the EUREKA! $R = 400$ data set using HYDRA. We have left out the constraints on the *P*–*T* profile parameters for clarity. The constrained temperature profile is given in Fig. 10.

APPENDIX E: EQUIVALENT WIDTH FITTING TO UNBLENDED O I, C I, AND CH LINES

Teske et al. (2016) reported the equivalent widths (EWs) of unblended carbon and oxygen lines measured from Magellan II/MIKE (Magellan Inamori Kyocera Echelle) spectra of WASP-94 A and WASP-94 B (see their extended table 1), but did not report the absolute abundances derived from these measurements for the individual stars. To translate the WASP-94 A EWs (specifically the EWA-IR EWs) into abundances, we used the same methodology as described in that paper, via the curve-of-growth analysis within MOOG and the PYTHON wrapper QOYLLUR-QUIPU (q^2; first described in Ramírez, Meléndez & Asplund 2014). We included seven C I lines, three CH lines, and the O triplet lines (with non-local thermodynamic equilibrium corrections from Ramírez, Allende Prieto & Lambert 2007 that are built into q^2). We used a MARCS (Model Atmospheres with a Radiative and Convective Scheme) 1D local thermodynamic equilibrium stellar model with the stellar parameters and associated errors listed in Table 1 of this paper (from the Teske et al. 2016 WASP-94 B reference, isochrone $\log g$ analysis). To then calculate [C/H] and [O/H] values for WASP-94 A, we assumed the absolute C and O solar abundances from Asplund et al. (2021) and took the logarithm of the difference, i.e. $10^{(\mathrm{WASP94A-solar})}$. Different combinations of C and O abundance indicators from both these EW measurements and the synthesis fitting are averaged together to get an estimate of 0.68 ± 0.10 for the C/O ratio of WASP-94 A. This analysis can be reproduced using the EWs and stellar parameters given in Teske et al. (2016) using q^2.

This paper has been typeset from a TEX/LATEX file prepared by the author.